The Astrophysical Journal, 699:330–347, 2009 July 1 doi:10.1088/0004-637X/699/1/330

HIGH-RESOLUTION 5 μm SPECTROSCOPY OF TRANSITIONAL DISKS

C. Salyk[1], G. A. Blake[1], A. C. A. Boogert[2], and J. M. Brown[3]
[1] Division of Geolofgical & Planetary Sciences, Mail Code 150-21, California Institute of Technology, Pasadena, CA 91125, USA
[2] IPAC, NASA Herschel Science Center, California Institute of Technology, Pasadena, CA 91125, USA
[3] Max Planck Institut für Extraterrestrische Physik, Postfach 1312, 85741 Garching, Germany
Received 2008 December 22; accepted 2009 April 27; published 2009 June 11

ABSTRACT

We present high-resolution *M*-band ($\sim$5 μm) spectra of 14 transitional disks—circumstellar disks with an optically thick outer zone but an inner region significantly depleted of small dust grains—obtained with NIRSPEC on the Keck II telescope. We detect CO emission from nine disks, and show that for the majority of these systems, the emission originates in the depleted inner disk region. We find that the presence of high 5 μm veiling, strong CO emission, and high accretion rates are usually correlated, suggesting that at least two classes of transitional disks exist—those nearly completely cleared, and those only partially depleted, within their transition radius. *Cleared* inner disks are consistent with the presence of a close stellar companion, or with formation by photoevaporation. Of the cleared transitional disks, at least two (HD 98800 B and CoKu Tau/4) are known to be circumbinary with projected binary separations of several AU or less. *Partially depleted* inner disks most often have CO that extends to small ($\lesssim$1 AU) radii, but compared to "classical" disks the CO excitation temperature is lower and the emission radii are larger than that expected for dust sublimation. These disks are consistent with the presence of a giant planet, and inconsistent with having been formed by photoevaporation. Although the inner regions of such disks are vertically optically thin in dust emission, line-of-sight opacities from the star can be large, and the complex physical and chemical processes therein make it difficult to derive a fiducial CO abundance with respect to molecular hydrogen. Thus, CO *M*-band lines are best suited to providing lower bounds as to the total inner disk gas mass. Amongst the partially depleted sources, veiling measurements and CO emission models demonstrate a great diversity of inner disk gas content and gas/dust ratios, suggesting a variety of planet-forming environments.

Key words: planetary systems: protoplanetary disks – stars: pre-main sequence

1. INTRODUCTION

Planets, now known to be common companions of nearby Sun-like stars, are believed to originate in the disks of gas and dust that form around collapsing protostars as a consequence of angular momentum conservation. Circumstellar disks and planetary systems are both well studied, and the set of processes that convert one to the other have been fleshed out in some detail (e.g., Ruden 1999). However, the observational constraints on this process are few. The formation of terrestrial planets and giant planet cores occurs on small scales, which cannot easily be spatially resolved. Additionally, to date, no planet has been conclusively shown to exist inside a gas-rich circumstellar disk, largely because high radial velocity precision is difficult to achieve with highly variable young stars (Setiawan et al. 2008; Huelamo et al. 2008). The potentially $\sim$Jovian mass companions to HR 8799 (Marois et al. 2008) and Fomalhaut (Kalas et al. 2008) reside in young debris disks, and extending such results to gas rich systems would provide new laboratories for the study of planetary system formation.

With this background in mind, it is easy to understand the excitement that accompanied the discovery of systems like TW Hya and GM Aur (Koerner et al. 1993; Calvet et al. 2002). The spectral energy distributions (SEDs) of these disks show a deficit of flux in the near-IR that suggests a lack of material close to the star. At the same time, far-IR fluxes are much higher, so the outer disk is still relatively massive. Could these disks represent the transitional phase between classical circumstellar disks and planetary systems like our own? Although this question is still unanswered, GM Aur and TW Hya are often referred to as "transitional disks."

To date the term "transitional disk" has been adopted somewhat loosely to describe collections of young stars whose SEDs are depleted relative to classical disks, in one way or another. Although the word "transitional" implies an evolutionary characteristic, these disks are generally defined by observational signatures. One broad definition of transitional disks, as described by Najita et al. (2007), is used for SEDs in which the near- to mid-IR fluxes are below typical "classical" levels. Another, which is the definition we will adopt here, refers to a subset of these objects—those with lower than typical fluxes in the near-IR but with steep rises in flux toward the far-IR. These peculiar SEDs suggest not just that material has been removed from the disk, but that it has been removed selectively from a gap surrounding the star.

The actual mechanism for clearing out gaps in transitional disks is not yet known, but possibilities include photoevaporation (Hollenbach et al. 1994; Alexander & Armitage 2007), dynamical clearing by a stellar or planetary-mass companion (Calvet et al. 2002; Rice et al. 2003) and grain growth (Tanaka et al. 2005). However, the discovery of significant quantities of gas in the inner regions of the transitional disks LkCa 15, GM Aur, and TW Hya (Najita et al. 2003; Rettig et al. 2004; Salyk et al. 2007) suggests against photoevaporation for at least some transitional disks. Additionally, recently obtained images of LkHα 330 (Brown et al. 2008) demonstrate a sharp transition between the thin and thick disk regions, which would be difficult to produce with grain growth alone. The exciting possibility thus remains that the characteristics of some transitional disks are most readily explained by the presence of young giant planets.

Transitional disks may not represent a single phenomenon. Although sharing the characteristic SED "dip" in the near-IR, the class as a whole spans a wide range of other parameters. For example, in the sample presented here, accretion rates range from undetectable (CoKu Tau/4, D'Alessio et al. 2005) to nearly

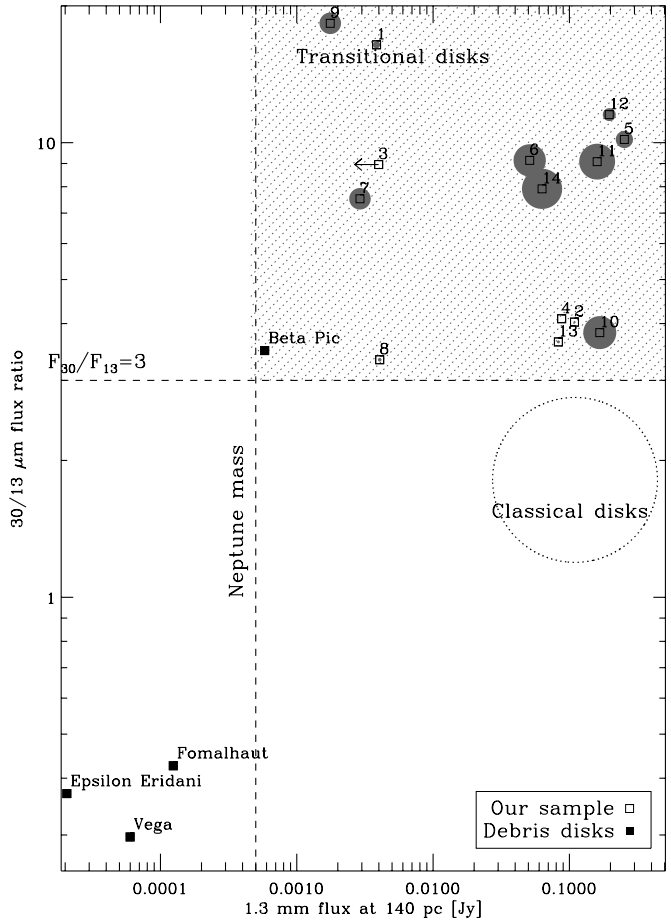

Figure 1. 30/13 μm flux ratios and distance-normalized 1.3 mm fluxes for the disks in our sample, as well as for four canonical debris disks. Filled gray circles have radii proportional to the size of the disk transition radius, if known. A dashed circle shows the typical fluxes and flux ratios for classical disks in Taurus. Dashed lines and hatched region delineate our selection criteria for transitional disks in this analysis. Flux corresponding to a Neptune mass disk assumes $\kappa_{1.3} = 0.02\,\mathrm{cm^2\,g^{-1}}$ and $T = 30$ K.

classical (GM Aur, Johns-Krull & Gafford 2002), disk gap sizes range from 3 AU (DM Tau, Calvet et al. 2005) to 56 AU (UX Tau A, Espaillat et al. 2007b), and total disk masses range from 1×10^{-4} to $2\times10^{-2}\,M_\odot$ (CoKu Tau/4 and DM Tau, respectively, Andrews & Williams 2005). As suggested by Alexander & Armitage (2007), the class of transitional disks may include both photoevaporated inner disks and systems that harbor giant planets, with the second process being more appropriate for sources with high accretion rates (i.e., TW Hya and GM Aur). Whether the variety amongst transitional disks reflects varied processes, stages of evolution, or population heterogeneity is an important question that remains to be answered.

With these issues in mind, we selected a varied group of 14 transitional disks to observe in the M band ($\sim5\,\mu$m) with NIRSPEC, a high-resolution echelle spectrograph on the Keck II telescope. The M-band region sits within the near-IR SED "dip," and thus the M-band excess continuum emission is produced largely by dust within the disk gap. Additionally, the M band harbors the P- ($\Delta J = +1$) and R-branch ($\Delta J = -1$) rovibrational transitions of CO. With upper state ($v = 1$) energies greater than 3000 K, producing these transitions thermally requires temperatures of at least several hundred K, meaning they are a good probe of the region within an AU or so from the host star. Indeed, these transitions appear to originate in a disk atmosphere at distances of $\sim$0.1–few AU (Najita et al. 2003; Blake & Boogert 2004; Pontoppidan et al. 2008). In this paper, we report the detection of CO rovibrational emission originating in nine out of the 14 observed transitional disks. For those with emission, we discuss the characteristics of the gas and its emitting region and implications for the formation of transitional disks. We also discuss the question of why some disks show emission and some do not, and how this relates to transitional disk diversity.

2. DESCRIPTION OF SAMPLE

The selection criteria for our sample of transitional disks are shown graphically in Figure 1. We were interested in studying those disks with depleted (optically thin) inner regions but optically thick outer disks. Accordingly, these disks tend to have a high 30/13 μm ratio (Brown et al. 2007) as compared to the median SED, but millimeter fluxes similar to classical disks. As selection criteria, we chose to include sources with $F_{30}/F_{13} \gtrsim 3$, and $F_{1.3mm} \gtrsim 0.0005$, which corresponds approximately to a Neptune mass of material (with $\kappa_{1.3} = 0.02\,\mathrm{cm^2\,g^{-1}}$ and $T = 30$ K). The use of F_{30}/F_{13} as a means of distinguishing transitional disks was introduced by Brown et al. (2007), but is in essence the same as the n_{13-25} criterion used to identify outliers in Furlan et al. (2006). This set of criteria is simple to apply because it is observationally based and does not require any model-based interpretation. The drawback of this approach is that it does not take into account other factors (such as grain opacity and stellar spectral type) that may determine whether or not the disk truly has an inner depleted region. Nevertheless, it does result in the inclusion of those transitional disks with confirmatory images of inner holes—a list that currently includes TW Hya (Hughes et al. 2007), LkHα 330 (Brown et al. 2008), GM Aur (Dutrey et al. 2008), SR 21, and HD 135344 (J. M. Brown et al. 2009, in preparation)—as well as HD 141569 A, which has had its inner hole resolved in CO emission lines (Goto et al. 2006). In addition, it does a fairly good job of excluding younger, optically thick classical disks, and more evolved debris disks. Interestingly, our selection criteria would permit the inclusion of Beta Pictoris, which, at a probable age of only $\sim$20 Myr (Di Folco et al. 2004, and references therein), may be transitioning from a primordial to a debris disk phase. The 1.3 mm fluxes were derived from the literature, or extrapolated from the closest known flux value assuming $F_\nu \propto \nu^2$ (Andrews & Williams 2005), while 30/13 μm flux ratios were calculated using *Spitzer* Infrared Spectrograph (IRS) spectra derived from Furlan et al. (2006), c2d data releases (Evans et al. 2003) or the *Spitzer* data archive.

Characteristics of the 14 selected transitional disks are summarized in Table 2. Sources derive from a variety of clusters, including Taurus, TW Hya, Serpens, and Ophiuchus. Additionally, they span spectral types from B9.5 to M1, accretion rates from undetectably low to $10^{-8}\,M_\odot\,\mathrm{yr^{-1}}$, and many orders of magnitude in disk mass. The sample thus represents a decent cross section of the T Tauri star population plus two Herbig Ae/Be stars, although with lower accretion rates than most classical T Tauri stars (cTTS's). Although all of the disks in our sample share the distinctive near/mid-IR SED "dip," followed by a subsequent rise in flux out to 20 μm or so (Jayawardhana et al. 1999; Calvet et al. 2002; Furlan et al. 2006; Brown et al. 2007), the location and size of the cleared-out gap, as well as the remaining mass in small dust grains, vary significantly from source to source.

Table 1
Summary of Observations

Star	Dates ($V_{\oplus}$[a])	Standards
CoKu Tau/4	2002 Dec (6), 2004 Dec (13), 2005 Dec (7), 2006 Dec (12)	HR 1620 [A7V]
DM Tau	2003 Nov (-14), 2005 Dec (9), 2006 Oct (−24), 2007 Mar (30)	HR 1620 [A7V], HR 1251 [A1V]
DoAr 21	2004 July (23)	HR 6175 [O9V]
DoAr 44	2004 July (23), 2005 April (−17)	HR 6175 [O9V], HR 6070 [A0V]
GM Aur	2004 Dec (11)	HR 1620 [A7V]
HD 135344	2005 Apr (−11), 2006 July (20)	HR 5712 [B4V], HR 5812 [B2.5V]
HD 141569 A	2002 Apr (−13), 2008 Jul (22)	HR 6175 [O9V], HR 5685 [B8V]
HD 98800	2001 Jan (−21)	HR 4635 [A1V]
HR 4796 A	2002 Apr (+2)	HR 4313 [A2V]
LkCa 15	2001 Jan (26)	HR 1620 [A7V]
LkHα 330	2002 Dec (11), 2003 Nov (-11), 2004 Dec (17)	HR 1177 [A3V], HR 1620 [A7V]
SR 21	2002 Apr (−19), 2006 Jul (17), 2007 Mar (−30)	HR 6175 [O9V], HR 5812 [B2.5V]
TW Hya	2001 Jan (−19), 2002 Apr (11), 2002 Dec (−24), 2005 Apr (12), 2004 Dec (−24), 2005 Dec (−24), 2006 May[b] (6)	HR 4313 [A2V], HR 4494 [B9V], HR 1620 [A7V], HR 2714 [A2V], HR 5028 [A2V]
UX Tau A	2006 Dec (14), 2007 Oct (−16)	HR 1620 [A7V]

Notes.
[a] Earth-induced Doppler shift in km s^{-1}. Add heliocentric Doppler shift of source to get shift between source and Earth's atmosphere. Measured heliocentric shifts: DoAr 44 (−2), GM Aur (20), HD 135344 (4), HD 141569 A (−17), LkHα 330 (15), SR 21 (−8),TW Hya (0), and UX Tau A (15).
[b] Observed with Phoenix.

Table 2
Our Sample: Stellar and Disk Properties

Star	SpT	Dist (pc)	$M_\star$ ($M_\odot$)	$R_\star$ ($R_\odot$)	$L_\star$ ($L_\odot$)	$T_\star$ (K)	i_d (°)	EW(Hα) (Å)	log $\dot{M}$ ($M_\odot$yr^{-1})	log $m_{\rm d}$ ($M_\odot$)	Index
CoKu Tau/4 [a]	M1[20]	140[b]	0.5[39]	1.9[c]	0.61[39]	3720 [39]	...	1.8–2.8[27]	<-11[14,k]	-3.3[3]	1
DM Tau	M1[20]	140	0.65[39]	1.2	0.25[39]	3720 [39]	32 ± 1 [41]	138.7[12]	-8.7[47]	-1.7[3]	2
DoAr 21	K1 [6]	119 [30]	1.3	1.6	32 [9]	5080	...	0.8 [6]	...	-3.5 [2,d,i]	3
DoAr 44	K3 [4]	119 [30]	1.2	0.8	2 [9]	4730	60 [4]	54–76.1 [40,9]	...	-2.4 [4]	4
GM Aur	K3[20]	140	1.2[39]	1.4	0.83[39]	4730 [39]	56 ± 2 [41]	71–109[28,16]	-8.0[25]	-1.5[3]	5
HD 135344	F4[44]	84[10]	1.6[44]	2.5	8.1[44]	6592[44]	14 ± 4 [36]	17.4[27]	-8.27[21]	-2.4[11]	6
HD 141569 A	B9.5 [31]	108 [31]	2.00 [31]	1.7	25.77 [31]	10000 [31]	51 ± 3 [46]	5.12 [5]	-11 [31]	-3.2 [31]	7
HD 98800 B[a]	K5 [34]	47.6 [18]	1.6 [34]	2.00 [34]	0.58 [34]	4000 [34]	66.8 ± 3.2 [8]	0.19 [15]	...	-8.2 [34,h]	8
HR 4796 A [c]	A0 [26]	67.1 [26]	2.4 [21]	1.7 [26]	21 [26]	9500 [26]	72^{+6}_{-9} [29]	...	<-8.53 [21]	-6.1 [22]	9
LkCa 15	K7 [42]	140	1.05 [1]	1.5	0.74 [1]	4350 [1]	57 ± 10 [42]	13–23.1 [28,27]	-8.8 [47]	-1.3[3]	10
LkHα 330	G3[10]	250[10]	2.5[10]	4.0	16.[10]	5800[10]	30^{+10}_{-10} [10,e]	11–20[27]	-8.8[19,f]	-1.4[11]	11
SR 21	G2.5[10]	160[10]	2.5[10]	4.9	24.[10]	5800 [10]	22^{+4}_{-4} [36]	0.54[27, g]	<-8.84[33]	-1.3[11]	12
TW Hya	K7[45]	51[17]	0.6[35]	1.0	0.25[42]	4060	4.3 ± 1.0 [36]	194. [37]	-8.8[23]	-1.6[43,j]	13
UX Tau A	K5[20]	140	1.1[24]	1.4[24]	1.0[24]	4350	29[11]	4[7]	-9.0[32]	-2.3[3]	14

Notes.
References. (1) Akeson et al. 2005, (2) Andre & Montmerle 1994, (3) Andrews & Williams 2005, (4) Andrews & Williams 2007, (5) Andrillat et al. 1990, (6) Bary et al. 2003, (7) Beckwith et al. 1990, (8) Boden et al. 2005, (9) Bouvier & Appenzeller 1992, (10) Brown et al. 2007, (11) Brown 2007, (12) Cohen & Kuhi 1979, (13) Dent et al. 2005, (14) D'Alessio et al. 2005, (15) Dunkin et al. 1997, (16) Edwards et al. 1994, (17) Eisner et al. 2006, (18) Favata et al. 1998, (19) Fernandez et al. 1995, (20) Furlan et al. 2006, (21) Garcia-Lopez et al. 2006, (22) Greaves et al. 2000, (23) Herczeg & Hillenbrand 2008, (24) Johns-Krull et al. 1998, (25) Johns-Krull & Gafford 2002, (26) Jura et al. 1998, (27) Kessler-Silacci et al. 2006, (28) Kitamura et al. 2002, (29) Koerner et al. 1998, (30) Lombardi et al. 2008, (31) Merín et al. 2004, (32) Najita et al. 2007, (33) Natta et al. 2006, (34) Prato et al. 2001, (35) Qi et al. 2004, (36) Pontoppidan et al. 2008, (37) Reipurth et al. 1996, (38) de la Reza & Pinzón 2004, (39) Sargent et al. 2006, (40) Shevchenko & Herbst 1998, (41) Simon et al. 2001, (42) Thi et al. 2004, (43) Trilling et al. 2001, (44) van Boekel et al. 2005, (45) Webb et al. 1999, (46) Weinberger et al. 1999, and (47) White & Ghez 2001.
[a] Binary — properties for a combined system.
[b] Taurus distances are taken to be 140 pc.
[c] Stellar parameters without references are calculated from other parameters.
[d] Upper limit.
[e] Adopted for SED fitting; not well constrained.
[f] Estimated from full width of Hα at 10% level and Equation (1) of Natta et al. (2004).
[g] Absorption.
[h] Lower limit.
[i] Assuming $\kappa_{1.3\,\rm mm} = 0.02\,{\rm cm^2\,g^{-1}}$ and $T = 30\,{\rm K}$.
[j] Corrected for the distance.
[k] Estimated upper limit based on Muzerolle et al. (2000).

Several of our sources are members of multiple star systems. HD 135344, HR 4796 A, and SR 21 are all in wide binary systems with separations of 20.″4 (Coulson & Walther 1995), 7.″7 (Jura et al. 1993), and 7.″8 (McCabe et al. 2006), respectively. HD 141569 A is a member of a triple system with A–B separation of 7.″5 and B–C separation of 1.″5 (Rossiter 1943; Weinberger et al. 2001). For all of these sources, the *Spitzer* spectrum should have included only the primary, and only the primary was observed with NIRSPEC. UX Tau is a quarternary system, with A–B and A–C separations of 5.″86 and 2.″63, respectively, and with B a subarcsecond binary. Thus *Spitzer* photometry and spectra include 2–4 of the components, depending on the wavelength band and observing mode (Furlan et al. 2006). While the A component is classified as a cTTS, the B and C components are classified as weak-line T Tauri stars (wTTS's). In addition, the A flux dominates over that from B and C by factors of 7 and 24, respectively, at 3.6 μm (White & Ghez 2001). Therefore, a circumstellar disk around the A component is the likely source of the emission observed with *Spitzer*. Our spectra, too, are dominated by only one component, presumably UX Tau A.

HD 98800 B is a member of a quadruple system with an A–B separation of 0.″8 (Koerner et al. 2000). Both components are themselves spectroscopic binaries with separation 23.7 mas ($\sim$1 AU; Boden et al. 2005). For this source, the disk is circumbinary, and the "transitional-like" SED is a result of tidal truncation due to the binary orbit (Furlan et al. 2007). Similarly, for CoKu Tau/4, a 53 mas ($\sim$8 AU) binary, the SED-derived transitional radius is consistent with dynamical clearing from the binary pair (Ireland & Kraus 2008). Although these disks are circumbinary and so not physically in transition, we explicitly include them here for the purpose of comparison.

The resulting sample encompasses most of the bright transitional disks that have been discussed in the literature and are observable from Mauna Kea. Some notable exceptions include disks with depleted inner disks, but no significant rise out to longer wavelengths—for example, Hen 3–600 A (Uchida et al. 2004) and v819 Tau (Calvet & D'Alessio 2001). Transitional/debris disks that fit our criteria but are not observable due to their low declination include T Cha (Brown et al. 2007) and β Pic. Further, we are effectively limited to *M*-band fluxes $\gtrsim$ 0.01–0.1 Jy, and so our set of observations becomes less complete for later-type sources and for more distant clusters. For example, we have not fully investigated the possibly transitional disk-rich IC 348 cluster in Perseus (Lada et al. 2006; Muzerolle et al. 2006). *M*-band observations were previously reported for at least four sources in our sample: LkCa 15 (Najita et al. 2003), HD 141569 A (Brittain et al. 2003; Goto et al. 2006), TW Hya (Rettig et al. 2004; Salyk et al. 2007), and GM Aur (Salyk et al. 2007).

3. OBSERVATIONS AND REDUCTION

The 14 transitional disks in this study were observed over a period of five years (from 2002–2008, see Table 1) with NIRSPEC (McLean et al. 1998), a high-resolution echelle spectrograph on the Keck II telescope. Spectra were obtained in the *M*-band region, with a 0.″43 × 24″ slit, providing a resolution of $R\sim$25000 (FWHM$\sim$12.5 km s^{-1}). Two spectral orders typically spanning 4.65–4.78 and 4.96–5.1 μm were obtained. LkCa 15 and HD 98800 B were observed over a smaller range, while GM Aur, LkHα 330, and TW Hya were observed over a slightly more extended range. These wavelength ranges encompass R(0–1) and P(1–12, 30–40) (or R(0–5) and P(26–43) in the extended cases) of the fundamental ($v = 1\rightarrow0$) rovibrational transitions of CO, as well as portions of the $v = 2 \rightarrow 1$ spectrum and ^{13}CO P and R branches. Additionally, the spectra encompass 2–3 H I electronic transitions: Pfβ (4.654 μm), Huε (4.673 μm), and Huδ (5.129 μm).

Spectra were recorded in ABBA sets, with each image acquisition (integration time plus co-adds) limited to one minute, in order to minimize atmospheric changes between the AB pairs. Data were reduced using IDL routines. AB pairs were subtracted to remove thermal noise, linearized and summed along the slit direction to create one-dimensional spectra. The one-dimensional spectra were then aligned using telluric emission lines, weighted according to S/N and summed. Telluric lines were also used for wavelength calibration, while standard stars served to correct for atmospheric absorption. Stars of type A and earlier were chosen because of their relatively few photospheric features at 5 μm. Nevertheless, the cooler stars do have prominent Pfβ absorption. To correct for this, these stars were divided by a Kurucz model, which was broadened to match the appearance of the Pfβ line. These corrections were all examined manually and are quite successful at removing Pfβ, with any possible remaining structure being less than a few % of the continuum.

After an adjustment for air mass, source spectra were divided by the standard star spectra. A final alignment of less than one pixel between source and standard was typically required to maximize S/N; this is likely due to small shifts in telluric emission line centers between images due to grating jitter. Flux calibration was performed by comparing sources and standards, along with standard star K magnitudes and spectral types. Flux calibration is not always reliable, because position shifts and changes in seeing can affect the throughput. To minimize this effect, slit positioning was constantly monitored and adjusted while observing, and the brightest spectra of standards and sources were chosen (i.e., spectra in which the stars were best centered). Continuum fluxes were compared at regions of low atmospheric absorption. Absolute flux calibration is generally accurate to within $\sim$20%, though there is never a guarantee that the discrepancy is not higher for a particular observation.

Data quality is primarily limited by the quality of the atmospheric absorption corrections. For our analysis, we removed spectral regions with very low atmospheric transmission by qualitatively analyzing individual spectra to decide the transmission threshold, which was typically in the range of 40%–70%. Since source CO emission will lie near or atop atmospheric CO absorption, it is helpful to observe at significant Doppler shifts. However, it was not always possible to avoid some overlap between source and telluric lines. Thus, spectra were also obtained at multiple Doppler shifts, when possible, to "fill-in" a complete spectrum (see Table 1). Spectra from different nights were averaged together, after small manual flux adjustments, to create the spectra shown in Figures 2 and 3. CO emission showed no significant night-to-night variations in line/continuum ratios, but 20% Pfβ flux variations were observed for DoAr 44 and TW Hya. Thus, this analysis uses an averaged version of the Pfβ emission line.

Spectra of TW Hya in a more limited wavelength range, but with significantly higher spectral resolution (measured FWHM$\sim$5 km s^{-1}) were obtained with Phoenix (Hinkle et al. 2003) on Gemini South. Spectra were obtained on 2006 April 6–7 using the 0.″25 × 14″ slit, and were reduced using the procedures outlined above (Salyk et al. 2007).

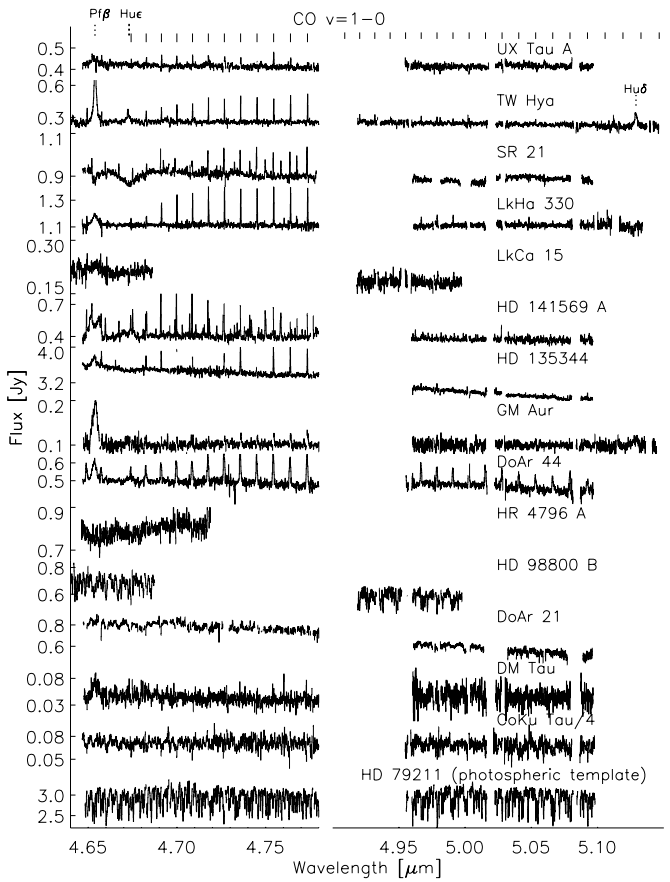

Figure 2. Spectra of the 14 transitional disks in our sample, plus one of our photospheric standards, in the first *M*-band order. CO $v = 1 \rightarrow 0$ emission lines are indicated above. ^{13}CO lines and $v = 2 \rightarrow 1$ lines are also present in the spectra of SR 21 and HD 141569 A. H I recombination lines Pfβ, Huδ, and Huε are also labeled.

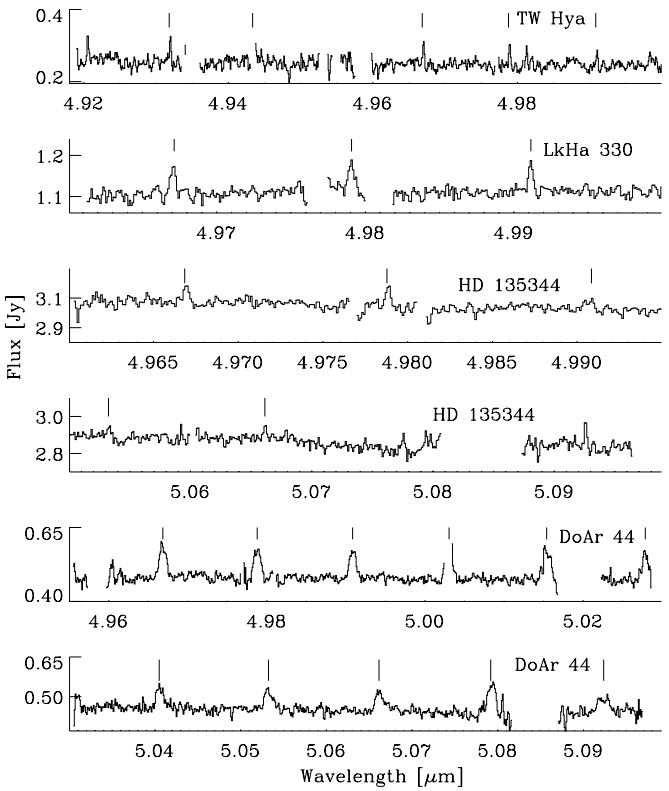

Figure 3. Close-up of lines longward of P(25). Note the different plot ranges for each source.

4. OVERVIEW OF SPECTRA

The complete set of reduced transitional source spectra is shown in Figures 2 and 3. We have also plotted the spectrum of one of our photospheric template stars (discussed further in Section 5). Of these disks, nine have detectable CO emission lines: DoAr 44, GM Aur, HD 135344, HD 141569 A, LkCa 15, LkHα 330, SR 21, TW Hya, and UX Tau A. Five disks do not have detectable CO emission at our achieved level of sensitivity: CoKu Tau/4, DM Tau, DoAr 21, HD 98800 B, and HR 4796 A. Note that the line detections for LkCa 15 are weak, but were previously detected across a larger wavelength range by Najita et al. (2003).

In Figure 4, we show the number of disks with CO and Pfβ detections, neither CO nor Pfβ, and Pfβ but no CO, separated by the accretion rate. The presence of CO emission is very strongly correlated with the presence of H I Pfβ emission, with DM Tau being the only source with Pfβ but no CO. This is consistent with both emission signatures arising from the inner disk. We also show that strong accretors always have Pfβ emission, and usually have CO emission, while only one of two weak accretors have CO emission. Additionally, for the set of sources with a weakly constrained or unknown accretion rate, the presence of CO and Pfβ is correlated with the strength of Hα. Although HD 141569 shows CO emission and has a low accretion rate, its CO emission does not arise from the inner disk, as we will show in Section 7.0.2.

CO-emitting sources tend to have relatively structureless continua, while many non-emission sources have stellar photospheric features. This qualitative grouping is also consistent with IR photometry, with emission sources having significant excess emission at or near 5 μm, while most non-emission sources have little or no 5 μm excess (e.g., Jayawardhana et al. 1999; Calvet et al. 2002; Furlan et al. 2006; Brown et al. 2007). In Figure 5, we plot the distance normalized CO line flux against *M*-band excess flux (discussed in Section 5). Note that HD 135344, HD 141569, and HR 4796 A are not included in this plot for reasons discussed in Section 5. The correlation between these two parameters suggests some co-evolution of gas and dust in transitional inner disks.

Note that the CO emission typically peaks shortward of 4.8 μm and is either absent or much weaker in the longer wavelength order. If gas densities are high enough, ^{13}CO emission can be observed; however, only two of our sources (HD 141569 A and SR 21) have detectable ^{13}CO emission. In addition, if temperatures and densities are high enough and/or if nonthermal processes such as UV pumping are important, one may expect to detect hot-band (v=2→1) CO emission. This is observed around HD 141569 A and SR 21 but no other stars in our sample; this is in contrast to classical T Tauri stars, for which strong CO-emitting sources have both fundamental and hot-band emission lines (Najita et al. 2003). CO also appears in absorption around SR 21 (for R(0) and R(1), and possibly part of the P-branch). This likely arises from cool foreground material, as SR 21 has a low-inclination (i.e., nearly face-on) disk.

5. THE 5 μm CONTINUUM

Although transitional sources are defined in part by their low excess flux in the near-IR, even a quick look at their *M*-band

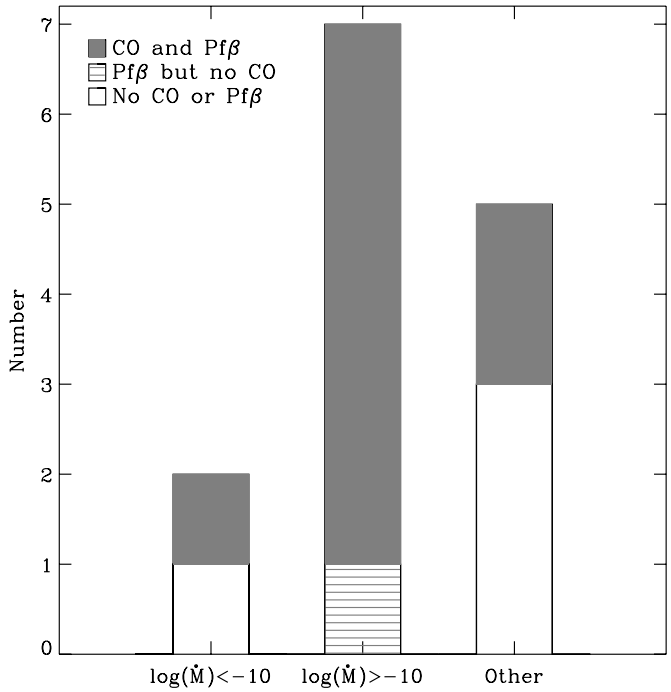

Figure 4. Histogram showing the numbers of disks with CO and Pfβ detections, neither CO nor Pfβ detected, or Pfβ but no CO. The three columns show low and high $\dot{M}$ sources ($[\dot{M}]=M_{\odot}$ yr^{-1}), respectively, followed by those for which $\dot{M}$ is either unknown or has only weak upper limits.

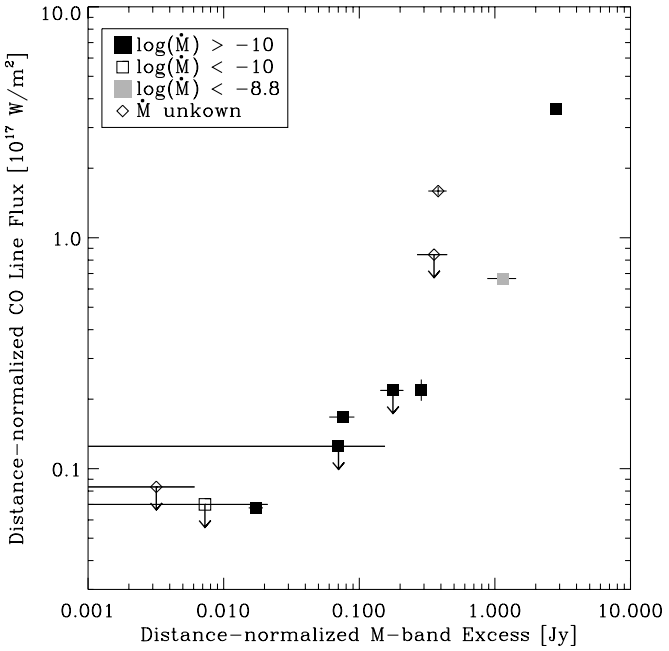

Figure 5. Comparison between CO line flux and M-band continuum excess, with both normalized to a distance of 140 parsecs. M-band continuum fluxes and error bars are taken from Table 4. CO line fluxes are the mean of P(6)–P(12), and error bars represent the standard error of the mean. Upper limits are shown for sources with no CO emission, assuming a 3σ detection limit and a line width (FWHM) of 15 km s^{-1}.

spectra reveals that many are far from photospheric at 5 μm. The infilling of photospheric features is referred to as veiling, and is defined as the ratio of continuum to photospheric flux ($r = F_{\rm cont}/F_{\rm phot}$). An understanding of the 5 μm veiling can be important for measurements of CO line fluxes, as well as interesting in its own right. Veiling measurements are crucial for accurately determining the dust content of the inner disk, as infrared excess emission can only be measured precisely if the flux contribution from the stellar photosphere is well characterized. In addition, observations of veiling at several wavelengths can be used to study the source of the excess.

Previous studies of veiling in classical T Tauri systems at shorter wavelengths (e.g., Hartigan et al. 1989; Folha & Emerson 1999; Johns-Krull & Valenti 2001; Muzerolle et al. 2003; Edwards et al. 2006; Eisner et al. 2007) have revealed at least two sources of veiling. These include a hot (several thousand K) component, correlated with various accretion proxies and therefore likely arising in the accretion column, and a cooler component (roughly ~1500 K) well fit as emission from a hot inner disk rim located at the dust sublimation radius. To our knowledge, no M-band veiling measurements have previously been published. As we will show, the 5 μm veiling in transitional sources may be consistent with emission from a slightly cooler dust component.

5.1. Fitting Method

Determination of veiling has been performed by a number of different methods, including examination of individual lines (e.g., Johns-Krull & Basri 1997), correlation analysis (Tonry & Davis 1979; Guenther & Hessman 1993; Folha & Emerson 1999), and point-by-point fitting (Hartigan et al. 1989). What all methods have in common is the idea that an observed spectrum consists of a scaled template photosphere and a constant or smoothly varying continuum. Determining the veiling at 5 μm presents a unique challenge because of the relatively lower S/N, the apparently large contribution from the continuum in many cases, and the complex nature of the photospheric features. Consequently, the veiling must be determined using a large number of points, and small numbers of outliers (for example, due to poor sky correction) can artificially cause large changes in the results. Except for qualitatively distinguishing the end-member cases, it is difficult to confirm the resulting fits by eye. Therefore, we use a modified version of a standard technique, which helps us characterize the systematic uncertainties in our fits.

We began by removing the CO emission regions from each spectrum and assumed that the remaining spectrum consisted of a scaled photospheric template plus a constant term. Our photospheric templates were taken to be observed M-band spectra of standard stars HD 79210 [M0V], HD 79211 [K7V], HD 107146 [G2V] or ROX 43 A [G5], shifted by a velocity $v_{\rm rad}$ and then convolved with a stellar rotation profile with some $v \sin i$ and a limb-darkening coefficient of 0.6. We rebinned the standard star spectrum so that its wavelength values matched that of the source. We then performed a linear least-squares fit—i.e., we found the coefficients of the equation $y = Ax + b$, where y is the observed spectrum, x is the observed photospheric template, A is a scaling term, and b is a constant continuum. Finally, $v_{\rm rad}$ and $v \sin i$ were varied to minimize the residual sum of squares. Except for the fact that we solved for $v_{\rm rad}$ and $v \sin i$ iteratively, rather than explicitly, our method is equivalent to the correlation method; the scaling term in a linear least-squares fit is directly related to the correlation coefficient R by $A = R \times \sigma_y/\sigma_x$, where σ_x and σ_y are the standard deviation of the x and y values, respectively.

There are several ways in which analyses of this kind can produce slightly incorrect or even spurious results. Problems related to the data themselves include misalignment of flux

from different observations or in different orders, improper flat fielding or non-Gaussian noise (from sky subtraction, for example). To minimize these effects we split our spectra into four sections at the natural boundaries between observations, performed the fits separately on each component, and then computed a weighted mean. The fits were carefully examined to remove outliers (from bad pixels, cosmic rays, bad sky subtraction, etc.) This method has the added benefit that the true uncertainty in the parameters is reflected in the variation amongst the four measurements. To determine our final error bars, we computed the ratio of the standard deviation of the four measurements and the statistical uncertainties of the fit parameters and then used this to scale the statistical uncertainty in the weighted mean. In short, this amounted to multiplying the purely statistical error bar in the weighted means by factors of ∼2–6 times.

A more difficult issue to address is the effect of using an improper template, for example with a surface gravity or spectral type different from the source. Unlike with the data-related problems, using an improper template will always act to increase the continuum term, perhaps by as much as 10%–15% (Hartigan et al. 1989). To estimate the magnitude of this offset in our own data, we fit one template, HD 79210, with another, HD 79211. This fit produced a continuum term of about 10% of the photospheric flux. A correction at this level is somewhat smaller than the size of our error bars, but should be kept in mind, as it preferentially results in low photospheric fluxes and high continuum fluxes. We also attempted to fit each spectrum with a variety of templates, including those listed in Table 4, CoKu Tau/4 and a weak-line T Tauri star TWA 8a. In all cases, we chose the fit with the lowest amount of veiling.

For Herbig Ae/Be stars HD 141569 A and HR 4796 A, a lack of photospheric features at 5 μm made an analysis of this kind impossible. Therefore, these two sources are not included in the analysis. Additionally, we did not observe an F-type standard star, and so there was not an appropriate template star for HD 135344.

Finally, we wanted to derive actual flux values for the photosphere, so that we could compare the veiling results with stellar blackbody estimates. However, as discussed in Section 3, absolute flux calibration is not always reliable. Therefore, we used published flux values (see the last two columns of Table 4) to estimate an *M*-band flux by linearly interpolating between the two closest measurements. We then scaled both our photospheric and continuum terms so that their sum equaled the interpolated flux value.

5.2. Veiling Results

Our veiling fits are summarized in Table 4. It is interesting to note that the transitional objects as a group span a large range of *M*-band veiling values, representing perhaps different "hole" sizes or different degrees of inner disk clearing/grain growth. CoKu Tau/4, DM Tau, and HD 98800 B are consistent with having zero excess flux in the *M* band.

In Figure 6, we compare our veiling-derived excess fluxes with those obtained by subtracting a model photospheric flux from the measured *M*-band flux. HD 141569 A, HR 4796 A, and HD 135344 have been excluded from this plot. The photospheric models are derived from a grid of Kurucz model atmospheres (Kurucz 1993), linearly interpolated over $T_{\rm eff}$ and log(g) and adjusted for size and distance according to Table 2. We have also corrected for extinction, although corrections are less than 10% for all but SR 21 ($A_V = 9$; Brown et al. 2007) and DoAr 21 ($A_V = 6.2$; Chen et al. 1995). Corrections for these sources are 25% and 16%, respectively.

In general, the predicted and observed excesses agree to within the error bars, but for a few sources the *M*-band veiling is somewhat different than would be predicted from photometry. The most likely explanation for much of this discrepancy is the use of an inappropriate template photosphere. Another possible explanation for the discrepancy could be time variability of the *M*-band flux. Near-IR variability has frequently been observed (Carpenter et al. 2001; Eiroa et al. 2002) and could extend to the *M* band. We have also observed variability of the H I recombination lines Pfβ and Huϵ in our own sample. Additionally, the photospheric fluxes themselves could have been overestimated. This possibility was discussed in Cieza et al. (2005), who showed that T Tauri luminosities are often based on the false assumption of no *J*-band veiling, which results in an overestimate of luminosity. Further, spectrally resolved *K*-band interferometry of Herbig Ae stars shows evidence for significant continuum emission from hot gas—perhaps H^- (Eisner et al. 2009)—which would also provide *J*-band veiling.

A final possible explanation for the observed discrepancy, when fit continua are too high, could be a third emission source that is neither photospheric nor smooth, such as hot molecular gas. Although the details of such a source cannot be constrained by our data, we show in Figure 7 that hot molecular gas close to the star can form a pseudocontinuum at some wavelengths. However, it is unlikely to be the dominant source of veiling, since it produces large-scale structure between 4.5 and 5 μm that is not seen in our data.

It is likely that dust in the inner disk is providing most or all of the continuum veiling at 5 μm, and veiling measurements at multiple wavelengths can be used to constrain the dust temperature and thus location. To our knowledge, only three stars in our sample have published veiling measurements at other wavelengths: GM Aur, TW Hya, and LkCa 15. In Figure 7, we show the excess flux as a function of wavelength for our measurements and those previously published (Folha & Emerson 1999; Johns-Krull & Valenti 2001; Edwards et al. 2006; Espaillat et al. 2008). From the definition of veiling, we assume

$$F_{\rm excess} = F_{\rm X} \times \frac{r_{\rm X}}{1 + r_{\rm X}}, \quad (1)$$

where $r_{\rm X}$ is the veiling measured in filter X, and $F_{\rm X}$ is a published photometric flux in that same filter, or an interpolated flux value based on fluxes in neighboring filters. *Y*-, *J*- and *K*-band flux values are taken from Rucinski & Krautter (1983), Kenyon & Hartmann (1995), Webb et al. (1999), and Hartmann et al. (2005).

For LkCa 15, we show that a 1600 K blackbody—found to provide a good match to a *K*-band veiling spectrum (Espaillat et al. 2008)—underpredicts the *M*-band excess, and suggests that an additional emission source may be present. For TW Hya and GM Aur, we show blackbody continua which best fit the *M*- and *K*-band veilings, and best-fit 1400 K blackbody emission. Temperatures of ∼1400 K are characteristic of near-IR continuum emission from cTTS disks (Muzerolle et al. 2003), and correspond well with the expected dust truncation radius, due either to magnetospheric accretion or dust sublimation (Eisner et al. 2007). The excess emission for TW Hya and GM Aur is more consistent with slightly lower temperatures, which could imply that the disk truncation is not due to dust sublimation, but rather to magnetospheric or dynamic truncation. Finally, for TW Hya, we also plot the emission

Table 3
Summary of SED Fitting: Results from the Literature

Star	$M_{\rm in}$ (M)	$R_{\rm thin,out}$[a] (AU)	$R_{\rm wall,in}$[b] (AU)	Σ_0 [c] (g cm^{-2})	Ref.
CoKu Tau/4	0.0007[d]	10	10	6×10^{-6}	4
DM Tau	0.0007[d]	3	3	1×10^{-5}	3
DoAr 21	...	...	...	...	...
DoAr 44	...	...	...	...	...
GM Aur	0.02	5	24	3×10^{-4}	3
HD 135344	0.10	0.45	45	1×10^{-2}	1
HD 141569 A	...	...	30	...	9
HD 98800 B [e]	...	2	5.9	...	7
HR 4796 A	...	...	$\sim$30	...	8
LkCa 15 [f]	0.001[g]	5	46	1×10^{-5}	6
LkHα 330	0.24	0.8	50	1×10^{-2}	1
SR 21	0.10	0.45	18	2×10^{-2}	1
TW Hya	0.5	4, 0.8	4, 0.8	7×10^{-3}, 6×10^{-7}, 9×10^{-7}	2, 5, 10
UX Tau A [h]	...	...	56	...	6

Notes.
[a] Outer edge of an optically thin disk.
[b] Inner edge of an optically thick disk.
[c] Σ_0 is estimated dust surface density at 1 AU assuming $\Sigma = \Sigma_0(r/\mathrm{AU})^{-3/2}$, the inner radius equal to the sublimation radius (Equation (4)), and outer radius as given in Column 3. For LkCa 15, the inner radius is instead taken to be 0.15 AU. For TW Hya, the last two values of Σ_0 are obtained directly from listed references.
[d] Upper limit.
[e] The model for HD 98800 B contains an optically thin ring between 1.5 and 2 AU.
[f] The model for LkCa 15 also contains an optically thick ring between 0.12 and <0.15 AU.
[g] The optically thin region.
[h] The model for UX Tau A contains an optically thick region from 0.16 to <0.18 AU containing a maximum of 216 M.
References. (1) Brown et al. 2007, (2) Calvet et al. 2002, (3) Calvet et al. 2005, (4) D'Alessio et al. 2005, (5) Eisner et al. 2006, (6) Espaillat et al. 2007b, (7) Furlan et al. 2007, (8) Jura et al. 1998, (9) Marsh et al. 2002, and (10) Ratzka et al. 2007.

Table 4
Veiling Results

Star	Phot. Flux (Jy)[a]	Cont. Flux (Jy)	r_M	$\Sigma_{0,v}$ (g cm^{-2})[b]	Template	Ref. Flux (Jy)	Ref
CoKu Tau/4	0.07 $\pm$ 0.01	0.01 $\pm$ 0.01	0.1 $\pm$ 0.2	$\mathbf{(1^{+2}_{-1}) \times 10^{-7}}$	HD 79210	0.08	2
DM Tau	0.08 $\pm$ 0.08	0.07 $\pm$ 0.08	1 $\pm$ 2	$(2 \pm 2) \times 10^{-6}$	HD 79210	0.14	3
DoAr 21	0.3 $\pm$ 0.1	0.5 $\pm$ 0.1	1.6 $\pm$ 0.7	$(2.0 \pm 0.5) \times 10^{-5}$[d]	HD 79210	0.85	1
DoAr 44	0.0 $\pm$ 0.1	0.5 $\pm$ 0.1	...	$(1.9 \pm 0.3) \times 10^{-5}$[d]	HD 79210	0.53	1
GM Aur	0.04 $\pm$ 0.02	0.08 $\pm$ 0.02	1.8 $\pm$ 0.8	$(1.8 \pm 0.4) \times 10^{-6}$	HD 79211	0.12	2
HD 135344[c]	0.00 $\pm$ 0.05	2.25 $\pm$ 0.05	...	$(4.7 \pm 0.1) \times 10^{-6}$	HD 79211	2.26	4
HD 98800 B	0.52 $\pm$ 0.04	0.03 $\pm$ 0.03	0.05 $\pm$ 0.05	$\mathbf{(4 \pm 4) \times 10^{-8}}$	HD 79210	0.58	5
LkCa 15	0.05 $\pm$ 0.01	0.18 $\pm$ 0.03	3 $\pm$ 1	$(9 \pm 2) \times 10^{-6}$	HD 79210	0.24	3
LkHα 330	0.02 $\pm$ 0.03	0.88 $\pm$ 0.02	40 $\pm$ 40	$(1.79 \pm 0.05) \times 10^{-5}$	ROX 43 A	0.90	1
SR 21	0.2 $\pm$ 0.9	0.9 $\pm$ 0.2	3 $\pm$ 13	$(7 \pm 2) \times 10^{-6}$	ROX 43 A	1.13	1
TW Hya	0.11 $\pm$ 0.02	0.13 $\pm$ 0.01	1.1 $\pm$ 0.2	$\mathbf{(3.5 \pm 0.4) \times 10^{-7}}$	HD 79211	0.25	2
UX Tau A	0.09 $\pm$ 0.02	0.29 $\pm$ 0.02	3.3 $\pm$ 0.8	$(5.8 \pm 0.4) \times 10^{-6}$	HD 107146	0.37	3

Notes.
[a] Median of Ax, where x is the photospheric template and A is the scaling term. Error bars here and elsewhere are 1σ and do not account for template mismatches.
[b] Column density of dust at 1 AU, assuming optically thin emission, $T = T_\star(R_\star/2r)^{2/5}$, $\Sigma = \Sigma_d(r/\mathrm{AU})^{-3/2}$, $R_{\rm in}$ is the dust sublimation radius with $T = 1500$ K, $R_{\rm out}$ is taken from Table 3 and $\kappa_{5\mu\mathrm{m}} = 440\,\mathrm{cm}^2\,\mathrm{g}^{-1}$. Bolded values are the actual dust column (because $\tau < 1$), while nonbolded values are lower limits.
[c] No proper template available, so measurement may be unreliable.
[d] Outer radius taken to be 3 AU.
Spectral types of templates are: HD 79210: M0V, HD 79211: K7V, HD 107146: G2V, ROX 43 A: G5.
References. (1) Evans et al. 2003, (2) Hartmann et al. 2005, (3) Kenyon & Hartmann 1995, (4) Malfait et al. 1998, and (5) Prato et al. 2001.

expected from the simple disk model of Eisner et al. (2006); this model predicts slightly lower M-band veiling than is observed, but the results agree to within 2σ.

Since veiling measurements directly measure excess flux, and do not depend strongly on stellar model parameters (as is the case for SED fitting), they can provide strong constraints on the inner disk dust mass. A proper analysis of dust fluxes requires careful modeling combined with measurements at a variety of wavelengths, which is beyond the scope of this paper. However, our data can provide an estimate of the inner disk dust content for very optically thin disks (with $\tau < 1$ along all lines of sight from the star), or a lower limit of the dust content for

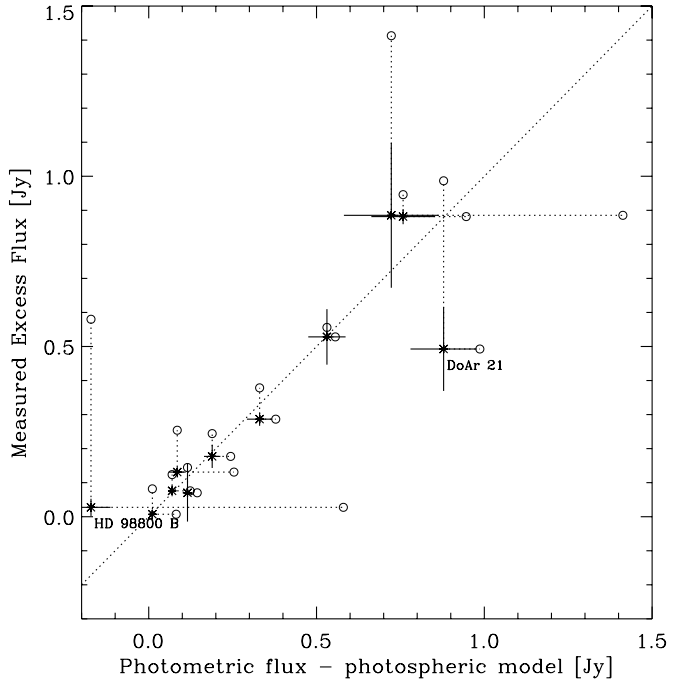

Figure 6. Comparison of veiling-derived excess flux (Equation (1)) and that derived from both photometry and stellar models (based on the parameters in Table 2). Veiling error bars are described in the text; photometric error bars are assumed to be 10%. The dashed line shows a 1:1 correspondence. Excess fluxes are by definition less than or equal to the total measured fluxes, which are shown as open circles at the end of dotted lines. Outliers from the 1:1 line are labeled for reference.

other disks. We assume the disk is everywhere optically thin to incoming radiation, such that

$$T(r) = \frac{1}{\epsilon^{1/4}} \left(\frac{R_\star}{2r}\right)^{1/2} T_\star, \quad (2)$$

where $\epsilon \sim (\lambda/a)^{-\beta}$ is the grain emissivity (Chiang & Goldreich 1997). For submicron-sized grains, $\beta \sim 1$ and a is similar to the peak stellar blackbody radiation, so $\epsilon \sim T/T_\star$ and

$$T(r) \approx \left(\frac{R_\star}{2r}\right)^{2/5} T_\star. \quad (3)$$

We also assume $\kappa_{5\mu} = 440$ cm^2 g^{-1}, $R_{\rm in} = R_{\rm sub}$ (see Equation (4)), $R_{\rm out}$ from Table 3, and $\Sigma = \Sigma_{0,v}\,(r/1\,{\rm AU})^{-3/2}$, where Σ is the dust mass surface density, and derive $\Sigma_{0,v}$—the veiling-derived dust mass surface density at 1 AU. See Table 4 for results.

Comparing our estimated inner disk dust contents with those estimated from SED fits (Table 3), we find that the results agree reasonably well for some sources (CoKu Tau/4 and the TW Hya result from Eisner et al. 2006), but in most cases it is an underestimate. Given the $\Sigma_{0,v}$ we derive, only CoKu Tau/4, HD 98800 B and TW Hya have $\tau \lesssim 1$ in the disk midplane, and so for all other disks, $\Sigma_{0,v}$ is a lower limit to the true disk dust content. For the three disks with $\tau \lesssim 1$, we confirm that the disk dust has been significantly depleted relative to a Minimum Mass Extrasolar Nebula disk with dust mass surface density $\Sigma_0 \sim 22$ g cm^{-2} (Kuchner 2004).

In the analyses that follow, we have utilized our best-fit photospheric templates to correct CO line fluxes for TW Hya. This correction could be underestimated if we have underestimated

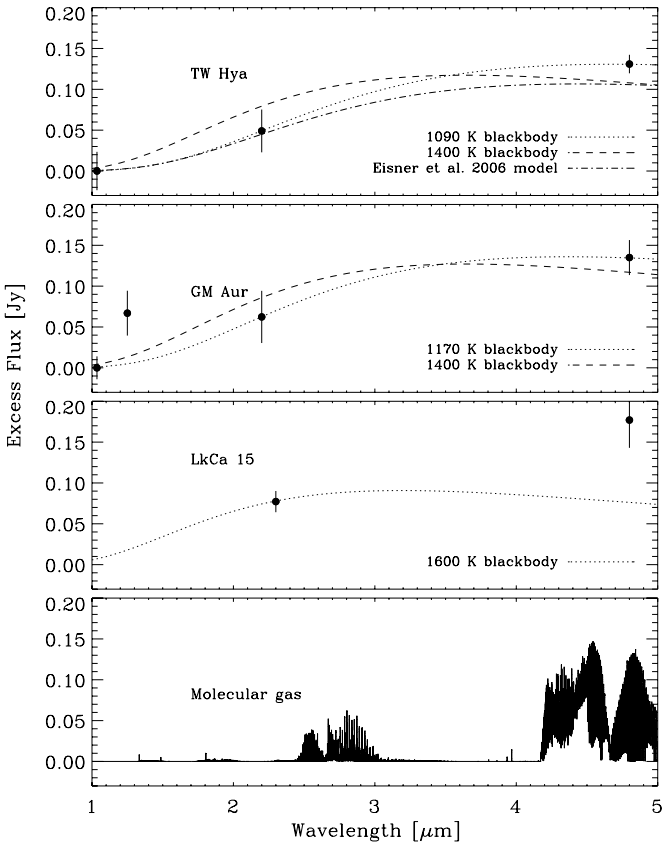

Figure 7. Top three panels show excess flux in the M (our work), Y, J, and K bands (Folha & Emerson 1999; Johns-Krull & Valenti 2001; Edwards et al. 2006; Espaillat et al. 2008), calculated with Equation (1). For LkCa 15, we plot the 1600 K blackbody found to fit the K-band continuum (Espaillat et al. 2008). For TW Hya and GM Aur, we plot blackbody continua that simultaneously fit the M- and K-band veiling measurements, as well as the best-fit 1400 K blackbody. For TW Hya, we additionally plot the emission expected from the simple disk model presented in Eisner et al. (2006). The bottom panel shows the emission expected from a gas consisting of CO (and ^{13}CO), H_2O, and CO_2 in the ratio 30:30:1. The temperature was set at 1500 K, emitting area at 1 AU^2 and column density of CO at 4×10^{20} cm^{-2}. Line shapes were taken to be 200 km s^{-1}, velocities comparable to Keplerian velocities near the surface of the star.

the photospheric flux contribution. However, even in the extreme case that all 5 μm continuum emission originates in a stellar photosphere, corrections are still modest and will not affect the overall conclusions of our work (Salyk et al. 2007). For all CO emission sources besides TW Hya, photospheric corrections were smaller than the measurement error and so no correction was applied.

6. H I RECOMBINATION LINES

Emission lines deriving from ionized hydrogen in the spectra of young stars are believed to arise in the magnetospheric interface between star and disk (see Calvet et al. 2000, and references therein). Although the line strength is related to the stellar accretion rate, the complexity of the environment typically precludes defining a simple relationship between the two. As the H I lines are not the main focus of our paper, we include only a qualitative exploration of the relationship between observed H I lines and other spectral diagnostics.

The full spectral region observed for this study included the Pfβ (4.654 μm), Huε (4.673 μm), and Huδ (5.129 μm) transitions. We see no evidence for H I emission in main

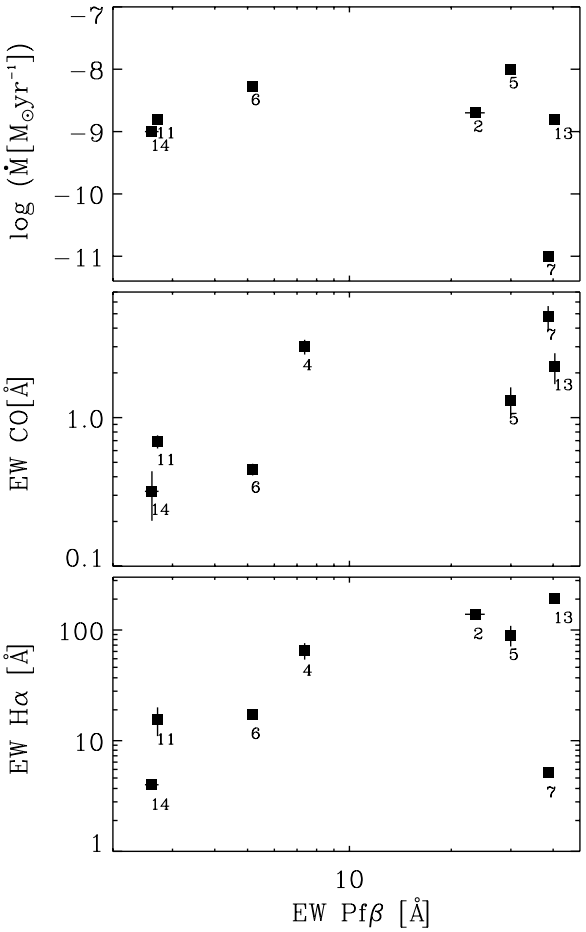

Figure 8. Pfβ equivalent width compared to the accretion rate (top), equivalent width of the CO v=1 → 0 P(6) line (middle), and Hα equivalent width (bottom).

sequence or weak-line T Tauri stars, and so all H I emission is assumed to derive from the accretion flow. Detection statistics and equivalent widths are shown in Table 5.

There is a correspondence between the accretion rate and the presence or lack of Pfβ emission. No clear correlation is seen between Pfβ equivalent width (or line luminosity) and accretion rates, although there is a moderate correlation between EW(Pfβ) and EW(Hα) (see Figure 8). This may be due to our small number statistics, opacity effects, or other complications. The lines also lack the blue asymmetries sometimes produced by inflow, but such asymmetries are not ubiquitous (see, for example, Muzerolle et al. 1998). Finally, line widths range from ~80 to 170 km s^{-1} values typical for H I lines originating in the magnetospheric inflow (Muzerolle et al. 2003).

As discussed in Section 4, we find a very strong correspondence between the presence of CO emission and Pfβ emission, with DM Tau as a possible exception. There is also a positive correlation between EW(Pfβ) and EW(CO), as seen in Figure 8. This is not too surprising, given that the inner gas disk is the reservoir for accreting material.

7. CO EMISSION LINE SHAPES

Spectrally resolved emission lines provide information about the velocity distribution of the gas from which they arise, as velocity along the line of sight causes Doppler broadening. The dominant velocity component for disks is from Keplerian motion (except for very face-on disks, where thermal or turbulent broadening can become important), and line shapes can be used to determine the inner extent of CO emission, R_{CO}. To extract spatial information from the line profiles, it was first important to confirm that they are spectrally resolved. NIRSPEC provides ~12.5 km s^{-1} sampling in the echelle mode, and average line widths for the six CO emitting sources are shown in Table 6. Errors are ~1–3 km s^{-1}. Since TW Hya's lines appeared only marginally resolved with NIRSPEC, additional spectra were obtained with Phoenix (FWHM ~5 km s^{-1}) on Gemini South. Details of the Phoenix observations are described in Salyk et al. (2007).

Table 5
H I Recombination Equivalent Widths

Source	Pfβ (Å)	Huε (Å)	Huδ (Å)
CoKu Tau/4	U	U	...
DM Tau	24 ± 2	U	...
DoAr 21	M	U	...
DoAr 44	7.4 ± 0.1	M	...
GM Aur	30.0 ± 0.6	M	M
HD 135344	5.2 ± 0.1	M	...
HD 141569 A	39.7 ± 0.3	15.4 ± 0.3	...
HD 98800 B	U	U	...
HR 4796 A	U	U	...
LkCa 15	M	U	...
Lk Hα 330	2.7 ± 0.1	M	...
SR 21	A	A	...
TW Hya	40 ± 0.4	8.0 ± 0.3	12.4 ± 0.4
UX Tau A	2.6 ± 0.1	U	...

Notes. An ellipsis means the wavelength of the transition was not observed. "U" means the region was observed, but no emission was detected. "M" refers to a marginal detection. "A" means the line is in absorption.

Table 6
CO Inner Radii

Source	FWHM[a] (km s^{-1})	R_{CO}[b] (AU)
DoAr 44	56	0.4 ± 0.1
GM Aur	42	0.5 ± 0.2
HD 135344	21	$1.1^{+0.9}_{-0.3}$
HD 141569 A	19	22^{+17}_{-7}
LkHα 330	19	13^{+3}_{-2}
SR 21	18	6^{+8}_{-2}
TW Hya	10	$0.1^{+0.2}_{-0.04}$
UX Tau A	31	2^{+2}_{-1}

Notes.
[a] Before instrumental deconvolution.
[b] Models assume $R_{out} = 50$ AU. Error bars represent a 95% confidence interval.

7.0.1. Constructing Line Composites

In order to increase emission line S/N and to "fill in" incomplete emission lines, we created line composites for each star. Although all lines should originate from the same approximate disk region, lower energy lines will be excited at somewhat lower temperatures. This preferentially increases the amount of low-velocity flux contributing to the lower energy emission line, making the line appear narrower. However, for most disks, we were unable to detect differences between lines of different energy, or between ^{12}CO, ^{13}CO, and overtone lines. For DoAr 44, there is a systematic increase in line width with excitation temperature, but no noticeable change in the

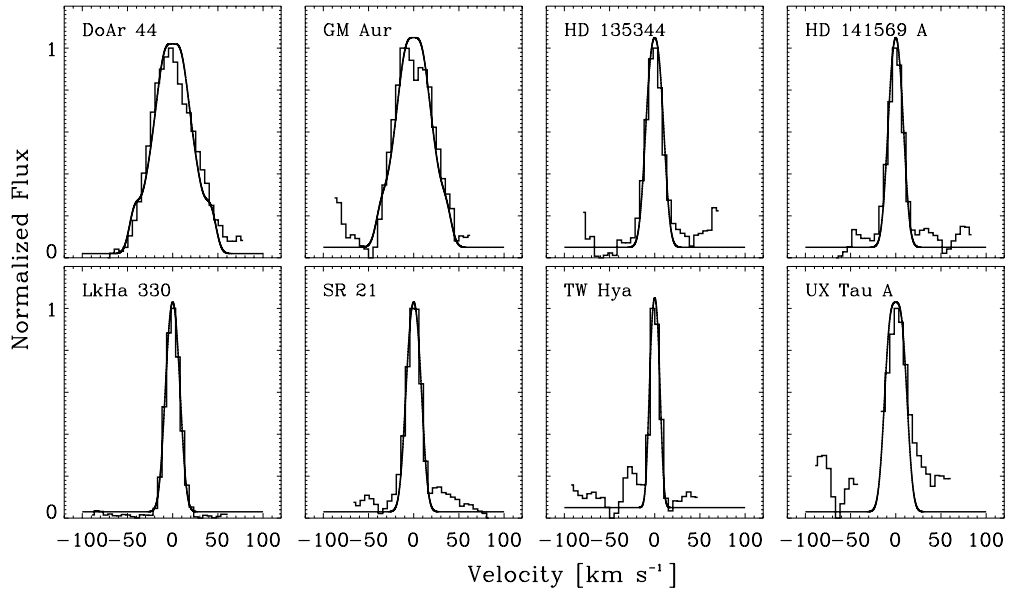

Figure 9. CO emission line composites. Fluxes have been continuum-subtracted and divided by their peak value. Solid curves show best-fit disk models used for the calculation of R_{CO}.

line shape. Therefore, we selected all clean, uncontaminated emission lines to create a single composite for each disk.

The following procedure was followed to construct the emission line composites. First, lines were extracted, centered using theoretical centers from the HITRAN database (Rothman et al. 2005), and converted to a velocity coordinate system. Then, lines were interpolated onto a 5 km s^{-1} grid (except for Phoenix lines, which were interpolated at a resolution of 2 km s^{-1}), and added together. Finally, lines were continuum-subtracted, and normalized to height 1. Note that this is slightly different from the procedure used in Salyk et al. (2007), in which lines were first normalized, then combined, and finally interpolated. This new procedure provides more weight for stronger (lower-excitation) lines. The complete set of line composites is shown in Figure 9.

7.0.2. Inner Radii

The CO emission line width is primarily determined by disk inclination and the inner radial extent of emitting CO molecules, but is also influenced by the disk density and temperature structure, as well as by any non-Keplerian motion in the disk. We have fit the emission with a simple disk model, in which the line emission originates in a disk surface with power-law temperature given by $T = 300(R/\mathrm{AU})^{-\alpha}$ K, and the inner (R_{CO}) and outer (R_{out}) radii are specified. We assume the gas is everywhere optically thin and normalize the peak flux to 1. We also set R_{out} to 50 AU. Radii beyond ~10 AU no longer contribute significant flux to the CO emission line, and so the model is insensitive to the exact value of R_{out}. Finally, we set $\alpha = 0.4$, the exponent expected for dust in a passive disk with submicron-sized grains (Chiang & Goldreich 1997). For DoAr 44 and GM Aur, however, models with $\alpha = 0.4$ were more double peaked than the data, but $\alpha = 0.2$ was found to yield a good fit.

Results are shown in Table 6 and Figure 9. Error bars represent the range of values in a 95% confidence interval, assuming a reduced χ^2 of 1 for the best-fit model. Note that the error bars do not include additional uncertainties in inclination and stellar mass. Also, the choice of α can have a substantial impact on the derived inner radius, with larger values of α corresponding to larger R_{CO}.

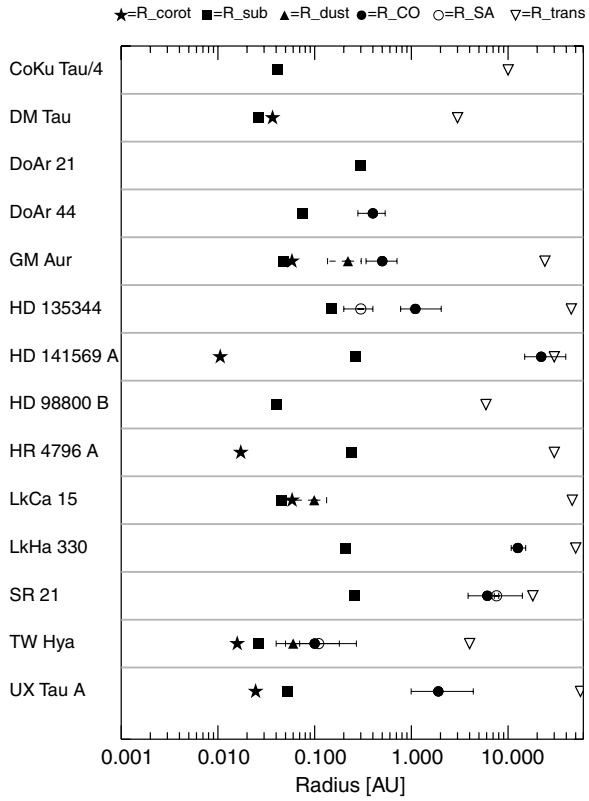

Figure 10. Comparison of several relevant disk radii: R_{corot}, R_{sub}, R_{dust}, R_{CO}, R_{SA}, and R_{trans} (details discussed in the text).

In Figure 10, we compare R_{CO} to other relevant disk radii: R_{sub}—the sublimation radius, R_{corot}—the stellar corotation radius, R_{dust}—the inner radius of the dust disk, R_{SA}—the CO inner radius derived from spectroastrometry, and R_{trans}—the radius of transition to an optically thick disk. R_{corot} is only provided for sources with published disk inclination and stellar $v \sin i$ (Clarke & Bouvier 2000; de la Reza & Pinzón 2004). R_{sub} is calculated assuming blackbody grains in a thin disk, with sublimation temperature 1500 K, but multiplied by a factor

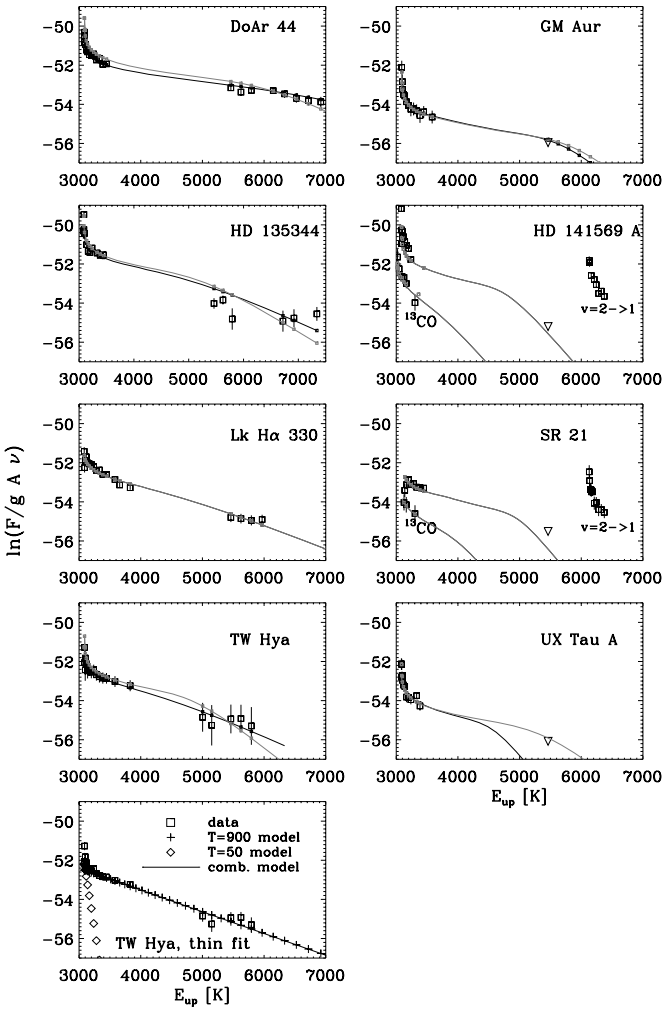

Figure 11. Rotation diagrams for the CO emission sources. The data points are usually nonlinear, which is indicative of large optical depths. Measured fluxes are shown as open boxes with error bars. Triangles are upper limits. Small, filled squares connected by solid lines are our best-fit models. Black is the overall best fit; gray is the best fit with a fixed emitting area. The bottom left panel shows the rotation diagram for the TW Hya fit with two optically thin components at different temperatures. The fit requires 10^{24} times as many cold molecules as hot.

of 1.5 to account for grain properties (see Akeson et al. 2005, for a discussion of how this factor varies amongst studies in the literature):

$$R_{\rm sub} = 1.5 \times 0.035 \times \left(\frac{L}{L_\odot}\right)^{1/2} \left(\frac{T_{\rm sub}}{1500}\right)^{-2}. \quad (4)$$

$R_{\rm dust}$ was measured via IR interferometry for GM Aur (Akeson et al. 2005) and TW Hya (Eisner et al. 2006). $R_{\rm trans}$ is taken from Table 3. For the purpose of comparison, we include all disks in our sample—even those from which no CO was observed. Note that sublimation radii are always much smaller than the transition radii, and so all disks are theoretically capable of harboring CO in the inner region. Also, there are no obvious structural differences between those disks with and without inner disk CO.

Our results are consistent with spectroastrometric results for SR 21 and TW Hya but slightly overestimated for HD 135344 (Pontoppidan et al. 2008), as well as for HD 141569 (11 ± 2 AU; Goto et al. 2006). $R_{\rm CO}$ is usually well within the transition radius, $R_{\rm trans}$, except for HD 141569 A and SR 21, where the two radii are similar. Therefore, for most but not all disks, the CO emission originates from well within the optically thin disk gap. $R_{\rm CO}$ should intuitively be similar to, or slightly larger than $R_{\rm dust}$, since the dust provides protection from UV dissociation. However, $R_{\rm CO}$ is often many times larger than $R_{\rm sub}$, in contrast to previous studies of cTTSs and Herbig Ae/Be (HAeBe) stars. For example, Najita et al. (2003) found that $R_{\rm CO}$ was within 0.5–$1 \times R_{\rm corot}$, and Monnier et al. (2005) found strong correlations between dust inner radii and sublimation radii for HAeBe stars. Eisner et al. (2006) calculated that the magnetic truncation radius is actually a few times larger than $R_{\rm corot}$, and suggested that this may explain the relatively large inner radius of GM Aur's dust disk. However, it is also possible that an entirely different mechanism may set the inner radius of transitional disks.

8. ROTATION DIAGRAMS

The strength of an emission line depends on both the temperature and amount of emitting gas, so variations in line flux with excitation energy are used to break this degeneracy. A convenient way to visualize this variation is with a rotation diagram, a plot of the log of the line flux—normalized by the state's degeneracy, Einstein A-coefficient and frequency—against the upper state energy. In the optically thin limit, they define a line with a slope of $-1/T_{\rm rot}$, where $T_{\rm rot}$ is defined as the rotational temperature, and an intercept proportional to $\ln(N\Omega)$, where N is the gas column density, and Ω is the solid angle subtended by the gas. $T_{\rm rot}$ is equivalent to the actual temperature of the gas if it is characterized by a single temperature and if the state populations are in thermal equilibrium. Deviations from linearity in rotation diagrams can result if the transitions are not optically thin, if the temperature is not constant throughout the material, or if there is nonthermal excitation of transitions—any of which can be true when considering emission from a circumstellar disk.

Rotation diagrams for eight of the nine CO emission sources are shown in Figure 11. LkCa 15 was not included in this analysis because too few lines were observed. The diagrams were constructed with the following procedure. First, all lines were fit with Gaussian distributions. An average line width was computed and combined with Gaussian heights to compute a total line flux for each line. In all cases, we assumed a constant continuum flux underlying the lines. Error bars were derived by adding the standard deviations of the line width and continuum flux in quadrature. Upper limits were computed for the ^{12}CO P(29) line (the lowest energy observable transition in the second M-band order) if no transitions were observed beyond $\lambda \sim 4.95\,\mu$m. They are shown as downward-pointing triangles in Figure 11. A prominent feature of all of the rotation diagrams is curvature at low energy, which may indicate temperature gradients, nonthermal excitations, or high optical depths.

The idea of explaining rovibrational fluxes as emission from optically thin gas components with different temperatures, or with a significant temperature gradient, has been discussed by Najita et al. (2003), Brittain et al. (2003), and others. In this case, the high excitation energy transitions would originate from a higher temperature gas and the lower excitation energy transitions from a lower temperature gas, producing steeper slopes at low excitation. However, given the steep dependence of flux on temperature, there must be a much larger mass of lower temperature molecules compared to higher temperature molecules in order to increase the flux in lower energy transitions significantly. This difference in mass required is not consistent

with the structure of circumstellar disks. We attempted to fit the rotation diagram with a power-law distribution of molecules ($N \propto T^{-q}$), as seen in circumstellar disks (Andrews & Williams 2007), but find that power laws cannot produce the sharp kink seen at ~3200 K. We rather find that a reasonable fit can be obtained with two components at $T = 900$ K and $T = 50$ K (see Figure 11). However, to produce enough 50 K flux, the ratio of numbers of molecules of the two components (cold/hot) must be 10^{24}. In contrast, in a disk with $\Sigma \propto r^{-1}$, the relative amount of mass from, say 0.05 to 0.1 AU as compared to that from 0.1 to 100 AU is only about 2000. Therefore, it seems unlikely that a typical circumstellar disk, in which mass is a decreasing function of radius, could produce significant rotation diagram curvature yet largely constant line profiles with upper state energy, if emission lines are thermally excited and the gas is optically thin.

The curvature could also be caused by nonthermal processes, such as by resonant scattering. This possibility is discussed in the context of HAeBe stars by Brittain et al. (2003) and Blake & Boogert (2004). We will show that, with the exception of HD 141569 A and SR 21, the line fluxes in our sample are well fit by a single temperature slab of moderate optical depth, in which the lower energy lines are optically thick but the higher energy lines are optically thin. For our analysis, we will assume the simplest case—that transitions are excited in a single temperature slab—as this allows for a qualitative understanding of the line emission. For those transitions that are optically thick, the ordinate in the diagram is determined primarily by the inverse of the degeneracy ($g = 2J+1$), causing significant curvature at low energies. The fluxes in the optically thick transitions depend on emitting area and temperature, while the optically thin transitions depend on column density and temperature. Thus if the transitions represent a variety of optical depths, the temperature, column density, and solid angle can all be constrained.

8.1. Model Description

In our simple slab model for CO emission, the gas sits in a flat disk with a single temperature T, column density N, and solid angle Ω (or area, if a distance is assumed). We assumed the local line broadening to be Gaussian with $\sigma = 2\,\mathrm{km\ s^{-1}}$—the sound speed for H_2 at 1000 K. (Note that this is different from Salyk et al. 2007, where the local line shape was assumed to be the same as the observed line shape. As a result, our current fits tend toward lower column densities.) We varied N, T, and Ω in order to fit the features of the rotation diagram, minimizing χ^2 to achieve the best fit. Our grid spacing for temperature was $\Delta T = 25$ K. For area, the gridding was $\Delta \log(\mathrm{Area[AU^2]}) = 0.08$ and for column density, the spacing was $\Delta \log(N[\mathrm{cm^{-2}}]) = 0.23$.

Multiple solutions exist for any given rotation diagram due to degeneracies between parameters (Najita et al. 2003; Salyk et al. 2007). To narrow the potential parameter space, we utilized a few additional constraints. One constraint is a column density upper limit imposed by the nondetection of ^{13}CO. To compute this limit, we assumed that ^{13}CO lines could be detected at the 2σ level above the background continuum. We then computed the ^{13}CO/^{12}CO line strength ratio at which the lines would be detectable, assuming an abundance ratio of 80/1. The line strength ratio is almost completely determined by the column density of the gas (with only a weak dependence on temperature), and so we determined a density limit. We also introduced a limit based on the assumption that the curvature at low rotational energies is real, and due to optical depth effects. χ^2 minimizations do not care about the order of the points, and therefore can allow fits that are clearly inappropriate when examined by eye. Our "curvature" limit required that the ordinate values for R(1) and P(13) differ by at least 1, thereby excluding very optically thin fits. A final limit was introduced for those sources with no detectable emission at P(29) or higher.

8.2. Model Fits

In general, a range of model fit parameters was allowed by the data, with low T fits corresponding to large N and large area and vice versa. Best fit T's ranged from 250 to 800 K, with a 95% confidence interval including T as high as ~1100 K for some sources, while best fit N's ranged from 10^{17} to 10^{20} cm^{-2}. Best fit areas ranged from as small as 0.02 AU^2 to as large as 78 AU^2 for sources with no detectable emission at P(29) or higher. We show the complete range of acceptable parameters, assuming a 95% confidence interval and the limits described in Section 8.1, in the top portion of Table 7. Note that the change in procedure as compared to Salyk et al. (2007)—as discussed in Section 8.1—results in slightly larger derived column densities, and a larger allowed range of parameters. The previously derived $\log(N)$ of 18.9 and 18.6 for GM Aur and TW Hya, respectively, lie within the ranges given in Table 7. Similarly, the previously derived temperatures of 550 and 750 K lie within the ranges derived here. However, the differences between various model fits underline the degeneracy of model parameters and the need for additional model constraints. Best-fit models are shown as black lines in Figure 11.

For future analyses, constraints on gas emission could be improved with more observations at higher excitation temperatures, or by constraining the emitting area with well resolved line shapes. To allow some comparative analysis between transitional disks, we present here best model fits with the area fixed at 0.23 AU^2—the best-fit area for LkHα 330, and an area for which most of the disks had acceptable fits. This small area was not compatible with the rotation diagrams for HD 141569 A and SR 21, and so for these two sources we instead fixed the area to the best fit value. Best-fit parameters are shown in the middle portion of Table 7 and are plotted as gray lines in Figure 11. χ^2 contours are shown in Figure 12.

For those disks from which no CO emission was observed, we calculated upper limits to the CO column density. We assumed $T = 400$ K, which is near the low end of the observed excitation temperatures, and emitting areas of 0.23 AU^2. We also assumed a 2σ detection threshold. For LkCa 15, we did not have enough data to constrain all model parameters, and so we fixed T and area for this source as well, to derive N.

8.3. The Special Case of HD 141569 A and SR 21

Neither HD 141569 A nor SR 21 were well fit by the isothermal model, and best model fits required unusually large emitting areas. Both of these disks have significant emission in higher vibrational states, and yet no $v = 1 \rightarrow 0$ emission in the second M-band order ($J \geqslant 29$), making an isothermal fit difficult. As discussed by Brittain et al. (2003) for HD 141569 A, this is indicative of UV pumping, in which electronic excitation of CO by stellar UV is followed by relaxation to vibrationally excited states. This effect also explains the characteristics of OH rovibrational emission from intermediate-mass stars (Mandell et al. 2008). With sufficient UV radiation from the accretion column, this may also explain the CO emission from SR 21. UV excitation is also consistent with our finding that the CO

Table 7
Excitation Diagram Fit Results

Star	Temp (K)	log(N_{CO}) (cm^{-2})	Area[a] (AU^2)		
DoAr 44	875–1325	18.0–18.9	0.012–0.037		
GM Aur	225–1125	16.6–19.7	0.002–94		
HD 135344 [b]	775	18.0	0.064		
HD 141569 A [b]	275	19.3	45.3		
LkHα 330 [b]	800	17.7	0.23		
SR 21	250–350	18.8–20.5	2.0–94		
TW Hya	350–1200	17.3–18.7	0.002–0.68		
UX Tau A	250–700	17.3–19.3	0.021–94		
Best Fits (Area Fixed)				log(Σ_{CO}/Σ_0)[c]	log($\Sigma_{CO}/\Sigma_{0,v}$)[d]
DoAr 44	625	18.9	0.23	···	1.3
GM Aur	400	19.7	0.23	1.0	3.1
HD 135344	575	18.5	0.23	−1.8	1.4
HD 141569 A	275	19.4	45	···	3.0
LkHα 330	800	17.7	0.23	−2.8	0.1
SR 21	250	19.9	78	−0.6	2.8
TW Hya	400	18.7	0.23	−1.5, 2.6, 2.4	2.8
UX Tau A	425	19.0	0.23	···	1.9
Upper Limits [e] (T, Area Fixed)					
CoKu Tau/4	400	16.1	0.23	−1.0	0.7
DM Tau	400	18.2	0.23	0.8	1.7
DoAr 21	400	17.1	0.23	···	−0.6
HD 98800 B	400	17.5	0.23	···	2.6
HR 4796 A	400	17.5	0.23	···	1.0
LkCa 15	400	17.1	0.23	−0.3	−0.2

Notes.
[a] Assuming distances in Table 2.
[b] No acceptable fits in a 95% confidence interval. Table entries are for best fit.
[c] Σ_0 from Table 3—SED results.
[d] $\Sigma_{0,v}$ from Table 4—veiling results.
[e] For LkCa 15, this is an estimate, not an upper limit.

emission arises at or near the transition radius—much further out in the disk than for the other stars in our sample.

Using a UV-excitation model, Brittain et al. (2007) derive a CO column of 10^{15} cm^{-2}, 4 orders of magnitude less than is found in our best isothermal fit. A factor of 100 can be accounted for by our smaller assumed emitting area, but the isothermal fit still overestimates the column density by two orders of magnitude, because it uses ^{13}CO/^{12}CO ratios as a density constraint. Therefore, the column density for SR 21 has also likely been overestimated by the isothermal fit.

8.4. Discussion of Rotation Diagram Results

Rotational temperatures are consistently higher than 250 K, and possibly as high as ∼1000 K. These temperatures are consistent with dust grain temperatures in the disk surface of planet-forming regions ($\lesssim$10 AU) around T Tauri stars. Gas temperatures decouple from dust temperatures in the disk atmosphere, and may reach values as high as ∼5000 K even at 20 AU (Kamp & Dullemond 2004), for a 4000 K star. However, since CO inner radii are also consistent with planet-forming distances (a few AU or less), this suggests that the CO and dust temperatures are similar, and that the emission does not originate far above the gas/dust coupling boundary ($\sim\tau = 1$). Collectively, the excitation temperatures for transitional disks are considerably lower than those found toward T Tauri (∼1200–1500 K, Najita et al. 2003) or Herbig Ae (∼800–1000 K, Blake & Boogert 2004) stars, in accordance with the larger emitting radii inferred from the line profiles.

In Table 7, we show CO/dust column density ratios computed using Σ_0 (the dust column density at 1 AU) derived from SED fitting, and $\Sigma_{0,v}$ derived from 5 μm veiling measurements. Because Σ_{CO} is a measure of hot gas, it represents a lower limit to the gas present. Nevertheless, using a fractional gas mass of $\sim 10^{-3}$ for CO, we see that GM Aur, and possibly TW Hya have gas/dust ratios that must be higher than the canonical 100/1 assumed for classical circumstellar disks. HD 135344 and LkHα 330, on the other hand, have significantly lower gas/dust ratios, with LkHα 330 in particular having the thinnest gas layer, and yet appearing heavily veiled. These results suggest that whatever the clearing mechanism for transitional disks may be, it does not affect all inner disks in the same way.

In Figure 13, we plot CO column densities against the total disk mass as derived from the millimeter-wave flux (leaving out HD 141569 A and SR 21, for the reasons discussed in Section 8.3). We do not see a correlation between the 1.3 mm flux and CO column, which would have suggested interaction between the inner and outer disks, or else a retention of information about initial conditions in the inner disk. However, we do see that the disks with no CO emission tend to have lower total disk masses. This suggests either that the disks with and without inner disk CO represent two different classes of disks, or else that the process which has depleted the inner disk of gas has also affected the outer disk. It is interesting to note that two

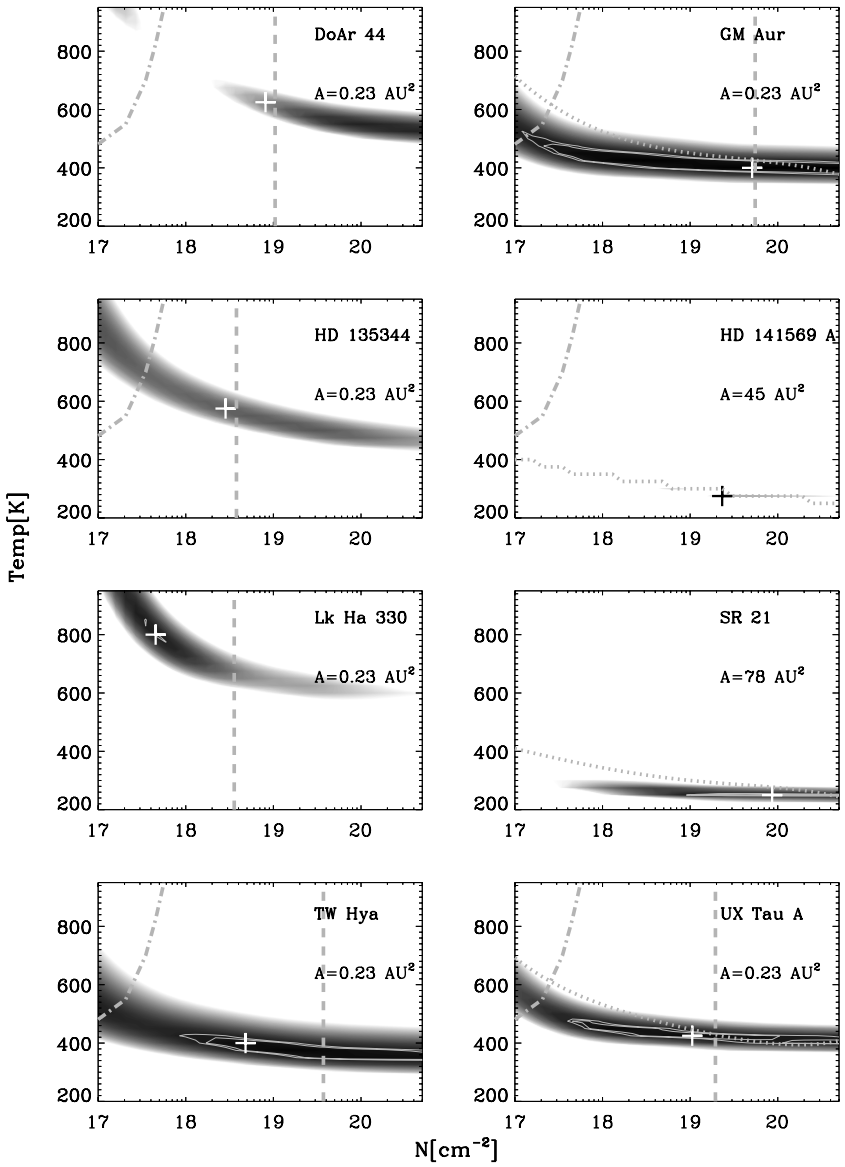

Figure 12. χ^2 plots of temperature and column density in our rotation diagram fits. Outlined contours are 95 and 99% confidence intervals. Dashed vertical lines represent density upper limits imposed by the nondetection of ^{13}CO. Dotted lines represent restrictions imposed by a nondetection of transitions at high rotational energy (P(29) or higher). Dash-dotted lines are restrictions imposed by the assumption that the curvature at low energy is real and due to optical depth effects. Note the tilt in the χ^2 contours, caused by the degeneracy of temperature and density.

of the disks with no CO detections, HD 98800 B, and CoKu Tau/4 are known close binaries, which, as a class, have lower disk masses (Andrews & Williams 2005).

The inner disk gas content can potentially be used to distinguish between different gap-opening mechanisms. For example, a disk with an inner optically thin region may be susceptible to the magnetorotational instability (MRI) transport, which predicts the following relationship between H_2 column density and accretion rate:

$$N \approx 5 \times 10^{24} \left(\frac{\dot{M}}{10^{-9} M_\odot \mathrm{yr}^{-1}}\right)^{3/4} \left(\frac{a}{\mathrm{AU}}\right)^{-3/4} \times \left(\frac{\alpha}{0.02}\right)^{-1} \hat{T}^{-1}\ \mathrm{cm}^{-2}, \quad (5)$$

where $\hat{T}$ is a constant > 1 that represents the superheating of disk gas over equilibrium blackbody temperatures (Chiang & Murray-Clay 2007). A standard α-disk model, in which the disk evolves through viscous dissipation, predicts (Pringle 1981)

$$\Sigma = \frac{\dot{M}}{3\pi\alpha\Omega H^2}. \quad (6)$$

A photoevaporating disk may potentially follow either of these relationships for radii inside of the critical radius for photoevaporative escape. However, such disks are also subject to the constraint that $\dot{M}$ be no higher than $\sim 10^{-10} M_\odot$ yr^{-1} (Alexander & Armitage 2007). In Figure 14, we show these relationships, as well as known values of $\dot{M}$, and Σ as derived from our CO column densities. We do not include HD 141569 A and SR 21, for the reasons discussed in Section 8.3. For simplicity, we assume a distance from the central star, a, of 1 AU (the approximate location of our CO emission) and a scale height, H, of 0.05 AU, and consider α ranging from 10^{-3} to 10^{-2}. In addition, we assume a constant fractional abundance of CO (x_{CO}) of 2×10^{-4} with respect to H_2. Note that in Salyk et al. (2007) we assumed the same x_{CO}, but mistakenly treated it as a mass ratio, and so the

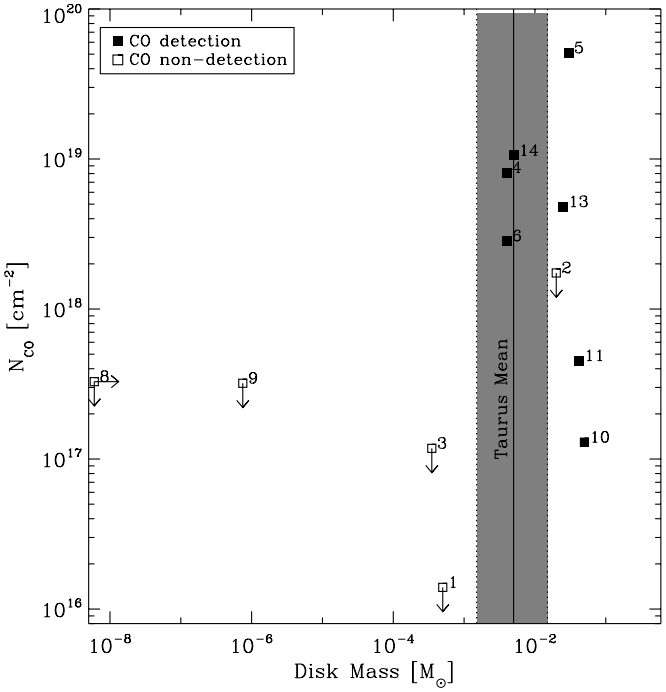

Figure 13. Plot of $M_{\rm disk}$ against $N_{\rm CO}$, with the latter derived from our rotation diagram fits. The Taurus mean, disk mass, and dispersion are shown by the shaded region (Andrews & Williams 2005). See Table 2 to find the source name corresponding to each index.

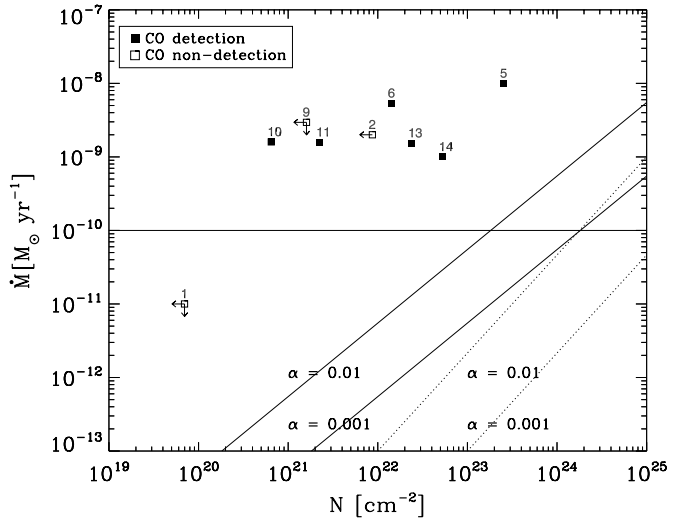

Figure 14. Plot of $\dot{M}$ against N—the gas column density—with the latter derived from our excitation diagram fits, assuming a CO abundance of 2×10^{-4}. Solid lines show the relationship expected for an α-viscosity disk model (Equation (7)); dotted lines show the prediction for MRI-driven accretion (Chiang & Murray-Clay 2007, Equation (5)). We show two different values of α, as labeled. The dash-dotted line shows the limit above which the accretion rate is too high to be consistent with photoevaporative clearing.

estimated gas mass densities given in our earlier paper should be reduced by a factor of 14.

The column densities we derive are significantly lower than that predicted by any of the equations described above. Because most of the inner disks are horizontally optically thick, CO emission probes only the upper disk atmosphere, and not the bulk of the disk gas. Furthermore, at low column densities the CO abundance is inversely related to the total column, and rather lower than the value assumed here (van Dishoeck & Black 1988). Thus, the gas columns and gas/dust ratios we derive are lower limits, and the actual range in Σ for these disks is likely to be smaller than that shown in Figure 14. Nevertheless, all sources with CO emission originating from well within the transition radius (i.e., all emitting sources besides HD 141569 A and SR 21) have CO column densities and accretion rates inconsistent with photoevaporative clearing of the inner disk.

9. DISCUSSION

We obtained 5 μm spectra of 14 transitional disks, selected to have high 30/13 μm ratios but "classical" disk masses. Of these disks, nine have detectable CO emission. By measuring the *M*-band veiling and CO emission features, we have investigated both the gas and dust components of the disk. Based on characteristic temperatures and emission radii, the CO emission appears to arise from well inside the transition radius for most disks, but at or near the transition radius for HD 141569 A and SR 21. The disks with CO emission inside their transition radii appear to differ in many ways from the disks without CO emission, and we suggest that they may represent two distinct classes of transitional disks. Disks with inner disk CO tend to have observable accretion rates and Pfβ emission, a high degree of veiling, as well as higher disk masses. A possible exception is DM Tau, with a high accretion rate, detectable H I recombination lines, and a high degree of veiling, but no detectable CO emission, to within our detection limits. Thus, many of the disks we observe have significant quantities of gas and dust within the transition radius and are actively accreting, while others have little or no detectable material in the inner disk. Of the class of "cleared" inner disks, two are known to be close binaries with circumbinary disks. If others turn out to be close binaries, searching for the presence of inner disk material, especially gas, may help distinguish between transitional SEDs formed by close stellar binaries versus planetary-mass companions.

Amongst those sources with CO emission, there is a great variety of CO line strengths and hence column densities. In addition, CO/dust mass ratios in the regions we probe vary greatly from disk to disk, suggesting a variety of inner disk environments. In our sample, a few disks especially stand out. LkHα 330 is heavily veiled, but has a CO column density one to two orders of magnitude lower than the other disks. It also has a relatively large CO inner radius. Has gas been preferentially removed by photoevaporation, or by accretion onto a gas giant? HD 141569 A and SR 21 are also interesting. These are the only two sources with ^{13}CO and CO 2→1 emission, are not well explained by a thermal emission model, and have large CO inner radii (∼10 AU). Why has the CO been cleared to such large radii in these disks, but not in most of the others?

All of the CO emission sources with good available photospheric templates have significantly veiled photospheres at 5 μm. Since 5 μm corresponds to the peak of a ∼600 K blackbody, the high degree of veiling suggests the presence of dust inside the transition radius. For three disks, GM Aur, LkCa 15, and TW Hya, veiling measurements have been made at other wavelengths. The dust emission is roughly consistent with an origin near the inner dust rim, though *M*-band excess flux may be somewhat higher than expected. Veiling measurements at several wavelengths thus provide constraints on the dust truncation radius that would otherwise require extremely high spatial-resolution measurements, such as those provided by optical or IR interferometry. Using additional veiling measurements, it

would be interesting to see if dust truncation radii are different for transitional disks than for classical T Tauri or Herbig Ae/Be disks, and to see if dust truncation radii differ greatly from disk to disk for stars of a given spectral type.

Do the inner disk gas and dust masses provide constraints on the formation mechanism for transitional disks? Disks with low-mass companions will not completely clear their inner regions of gas and dust (Artymowicz & Lubow 1996; Lubow et al. 1999), and so "partially depleted" transitional disks may be the best candidates for disks that harbor giant planets. Conversely, photoevaporation is expected to clear the inner disk on the viscous timescale, making observations of filled inner disks unlikely (Alexander & Armitage 2007). For those disks with nearly cleared inner regions, then, photoevaporation is a possible formation mechanism. However, two of the cleared inner disks observed in this study—CoKu Tau/4 and HD 98800 B—are binary pairs with circumbinary disks. The remaining cleared disks—HR 4796 A, DoAr 21 and possibly HD 141569 A—may still be potential candidates for photoevaporating transitional disks, or may also turn out to be circumbinary.

Unfortunately, it may prove difficult to distinguish between close stellar and planetary mass companions in transitional disks, as binaries display a variety of SEDs and accretion rates (e.g., Mathieu et al. 1994). CoKu Tau/4 and CS Cha, with projected separations of several AU (Ireland & Kraus 2008; Guenther et al. 2007), have transitional SEDs, with little or no near-IR excess (though CS Cha has an estimated accretion rate of $1.2 \times 10^{-8} M_{\odot}$ yr^{-1}; Espaillat et al. 2007a). DF Tau and GN Tau, on the other hand, have similar projected separations ($\sim$12 and $\sim$6 AU, respectively; Ghez et al. 1993; Simon et al. 1995) and yet have significant accretion rates or Hα equivalent widths (Mathieu et al. 1994) and nontransitional SEDs (Furlan et al. 2006). Nevertheless, thus far it seems that a cleared inner disk is a good predictor for a close binary with a circumbinary disk.

For those partially cleared transitional disks that may harbor giant planets, high-resolution spectroscopy will be instrumental for understanding disk/planet interactions, and exploring the complexity and seeming diversity of planet-forming environments. However, the challenge will be to relate what is observed in the upper disk atmosphere to the bulk properties of the inner disk. We have shown that even a simple single-temperature slab model cannot be well constrained by emission fluxes alone. To properly relate CO emission to column density, we will need to incorporate CO line production into a model that includes gas heating/cooling processes and CO dissociation. With these procedures in place, CO emission could provide key constraints on gap opening mechanisms and inner disk physics. More generally, high-resolution spectroscopy of additional atomic and molecular tracers should move us toward a better understanding of both the physics and chemistry in planet-forming regions of circumstellar disks.

The authors thank the anonymous referee for a careful reading of this manuscript, and acknowledge support from the NASA SIRTF and Origins programs. The data presented herein were obtained at the W. M. Keck Observatory, which is operated as a scientific partnership among the California Institute of Technology, the University of California and NASA. The Observatory was made possible by the generous financial support of the W. M. Keck Foundation. This work was also based in part on observations obtained at the Gemini Observatory, which is operated by the Association of Universities for Research in Astronomy, Inc., under a cooperative agreement with the NSF on behalf of the Gemini partnership. In addition, this work is based in part on archival data obtained with the *Spitzer Space Telescope*, which is operated by the Jet Propulsion Laboratory, California Institute of Technology under a contract with NASA.

REFERENCES

Akeson, R. L., et al. 2005, ApJ, 635, 1173
Alexander, R. D., & Armitage, P. J. 2007, MNRAS, 375, 500
Andre, P., & Montmerle, T. 1994, ApJ, 420, 837
Andrews, S. M., & Williams, J. P. 2005, ApJ, 619, L175
Andrews, S. M., & Williams, J. P. 2007, ApJ, 659, 705
Andrillat, Y., Jaschek, M., & Jaschek, C. 1990, A&A, 233, 474
Artymowicz, P., & Lubow, S. H. 1996, ApJ, 467, L77
Bary, J. S., Weintraub, D. A., & Kastner, J. H. 2003, ApJ, 586, 1136
Beckwith, S. V. W., Sargent, A. I., Chini, R. S., & Güsten, R. 1990, AJ, 99, 924
Blake, G. A., & Boogert, A. C. A. 2004, ApJ, 606, L73
Boden, A. F., et al. 2005, ApJ, 635, 442
Bouvier, J., & Appenzeller, I. 1992, A&AS, 92, 481
Brittain, S. D., Rettig, T. W., Simon, T., Kulesa, C., DiSanti, M. A., & Dello Russo, N. 2003, ApJ, 588, 535
Brittain, S. D., Simon, T., Najita, J. R., & Rettig, T. W. 2007, ApJ, 659, 685
Brown, J. M. 2007, PhD thesis, California Institute of Technology
Brown, J. M., Blake, G. A., Qi, C., Dullemond, C. P., & Wilner, D. J. 2008, ApJ, 675, L109
Brown, J. M., et al. 2007, ApJ, 664, L107
Calvet, N., & D'Alessio, P. 2001, in ASP Conf. Proc. 235, Science with the Atacama Large Millimeter Array, ed. A. Wootten (San Francisco, CA: ASP), 205
Calvet, N., D'Alessio, P., Hartmann, L., Wilner, D., Walsh, A., & Sitko, M. 2002, ApJ, 568, 1008
Calvet, N., Hartmann, L., & Strom, s. E. 2000, in Protostars and Planets IV, ed. V. Mannings, A. P. Boss, & S. S. Russell (Tucson, AZ: Univ. Arizona Press), 377
Calvet, N., et al. 2005, ApJ, 630, L185
Carpenter, J. M., Hillenbrand, L. A., & Skrutskie, M. F. 2001, AJ, 121, 3160
Chen, H., Myers, P. C., Ladd, E. F., & Wood, D. O. S. 1995, ApJ, 445, 377
Chiang, E. I., & Goldreich, P. 1997, ApJ, 490, 368
Chiang, E., & Murray-Clay, R. 2007, Nature Physics, 3, 604
Cieza, L. A., Kessler-Silacci, J. E., Jaffe, D. T., Harvey, P. M., & Evans, N. J., II 2005, ApJ, 635, 422
Clarke, C. J., & Bouvier, J. 2000, MNRAS, 319, 457
Cohen, M., & Kuhi, L. V. 1979, ApJS, 41, 743
Coulson, I. M., & Walther, D. M. 1995, MNRAS, 274, 977
D'Alessio, P., et al. 2005, ApJ, 621, 461
de la Reza, R., & Pinzón, G. 2004, AJ, 128, 1812
Dent, W. R. F., Greaves, J. S., & Coulson, I. M. 2005, MNRAS, 359, 663
Di Folco, E., Thévenin, F., Kervella, P., Domiciano de Souza, A., Coudé du Foresto, V., Ségransan, D., & Morel, P. 2004, A&A, 426, 601
Dunkin, S. K., Barlow, M. J., & Ryan, S. G. 1997, MNRAS, 290, 165
Dutrey, A., et al. 2008, A&A, 490, L15
Edwards, S., Hartigan, P., Ghandour, L., & Andrulis, C. 1994, AJ, 108, 1056
Edwards, S., Fischer, W., Hillenbrand, L., & Kwan, J. 2006, ApJ, 646, 319
Eiroa, C., et al. 2002, A&A, 384, 1038
Eisner, J. A., Chiang, E. I., & Hillenbrand, L. A. 2006, ApJ, 637, L133
Eisner, J. A., Hillenbrand, L. A., White, R. J., Bloom, J. S., Akeson, R. L., & Blake, C. H. 2007, ApJ, 669, 1072
Eisner, J. A., Graham, J. R., Akeson, R. L., & Najita, J. 2009, ApJ, 692, 309
Espaillat, C., et al. 2007a, ApJ, 664, L111
Espaillat, C., Calvet, N., D'Alessio, P., Hernández, J., Qi, C., Hartmann, L., Furlan, E., & Watson, D. M. 2007b, ApJ, 670, L135
Espaillat, C., Calvet, N., Luhman, K. L., Muzerolle, J., & D'Alessio, P. 2008, ApJ, 682, L125
Evans, N. J., II, et al. 2003, PASP, 115, 965
Favata, F., Micela, G., Sciortino, S., & D'Antona, F. 1998, A&A, 335, 218
Fernandez, M., Ortiz, E., Eiroa, C., & Miranda, L. F. 1995, A&AS, 114, 439
Folha, D. F. M., & Emerson, J. P. 1999, A&A, 352, 517
Furlan, E., et al. 2006, ApJ, S165, 568
Furlan, E., et al. 2007, ApJ, 664, 1176
Garcia-Lopez, R., Natta, A., Testi, L., & Habart, E. 2006, A&A, 459, 837
Ghez, A. M., Neugebauer, G., & Matthews, K. 1993, AJ, 106, 2005
Goto, M., Usuda, T., Dullemond, C. P., Henning, T., Linz, H., Stecklum, B., & Suto, H. 2006, ApJ, 652, 758
Greaves, J. S., Mannings, V., & Holland, W. S. 2000, Icarus, 143, 155

Guenther, E., & Hessman, F. 1993, A&A, 268, 192
Guenther, E. W., Esposito, M., Mundt, R., Covino, E., Alcalá, J. M., Cusano, F., & Stecklum, B. 2007, A&A, 467, 1147
Hartigan, P., Hartmann, L., Kenyon, S., Hewett, R., & Stauffer, J. 1989, ApJS, 70, 899
Hartmann, L., Megeath, S. T., Allen, L., Luhman, K., Calvet, N., D'Alessio, P., Franco-Hernandez, R., & Fazio, G. 2005, ApJ, 629, 881
Herczeg, G. J., & Hillenbrand, L. A. 2008, ApJ, 681, 594
Hinkle, K. H., et al. 2003, Proc. SPIE, 4834, 353
Hollenbach, D., Johnstone, D., Lizano, S., & Shu, F. 1994, ApJ, 428, 654
Huelamo, N., et al. 2008, A&A, 489, L9
Hughes, A. M., Wilner, D. J., Calvet, N., D'Alessio, P., Claussen, M. J., & Hogerheijde, M. R. 2007, ApJ, 664, 536
Ireland, M. J., & Kraus, A. L. 2008, ApJ, 678, L59
Jayawardhana, R., Hartmann, L., Fazio, G., Scott Fisher, R., Telesco, C.M., & Piña, R.K. 1999, ApJ, 521, L129
Johns-Krull, C. M., & Basri, G. 1997, ApJ, 474, 433
Johns-Krull, C. M., & Gafford, A. D. 2002, ApJ, 573, 685
Johns-Krull, C. M., & Valenti, J. A. 2001, ApJ, 561, 1060
Johns-Krull, C. M., Valenti, J. A., & Linsky, J. L. 1998, in ASP Conf. Ser. 154, Cool Stars, Stellar Systems, and the Sun, ed. R. A. Donahue & J. A. Bookbinder (San Francisco, CA: ASP), 1724
Jura, M., Malkan, M., White, R., Telesco, C., Pina, R., & Fisher, R. S. 1998, ApJ, 505, 897
Jura, M., Zuckerman, B., Becklin, E. E., & Smith, R. C. 1993, ApJ, 418, L37
Kalas, P., et al. 2008, Science, 322, 1345
Kamp, I., & Dullemond, C. P. 2004, ApJ, 615, 991
Kenyon, S. J., & Hartmann, L. 1995, ApJS, 101, 117
Kessler-Silacci, J., et al. 2006, ApJ, 639, 275
Kitamura, Y., Momose, M., Yokogawa, S., Kawabe, R., Tamura, M., & Ida, S. 2002, ApJ, 581, 357
Koerner, D. W., Jensen, E. L. N., Cruz, K. L., Guild, T. B., & Gultekin, K. 2000, ApJ, 533, L37
Koerner, D. W., Ressler, M. E., Werner, M. W., & Backman, D. E. 1998, ApJ, 503, L83
Koerner, D. W., Sargent, A. I., & Beckwith, S. V. W. 1993, Icarus, 106, 2
Kuchner, M. J. 2004, ApJ, 612, 1147
Kurucz, R. L. 1993, Kurucz CD-ROM (Cambridge, MA: Smithsonian Astrophysical Observatory)
Lada, C. J., et al. 2006, AJ, 131, 1574
Lombardi, M., Lada, C. J., & Alves, J. 2008, A&A, 480, 785
Lubow, S. H., Seibert, M., & Artymowicz, P. 1999, ApJ, 526, 1001
Malfait, K., Bogaert, E., & Waelkens, C. 1998, A&A, 331, 211
Mandell, A. M., Mumma, M. J., Blake, G. A., Bonev, B. P., Villanueva, G. L., & Salyk, C. 2008, ApJ, 681, L25
Marois, C., et al. 2008, Science, 322, 1348
Marsh, K. A., Silverstone, M. D., Becklin, E. E., Koerner, D. W., Werner, M. W., Weinberger, A. J., & Ressler, M. E. 2002, ApJ, 573, 425
Mathieu, R. D. 1994, ARA&A, 32, 465
McCabe, C., Ghez, A. M., Prato, L., Duchene, G., Fisher, R. S., & Telesco, C. 2006, ApJ, 636, 932
McLean, I. S., et al. 1998, Proc. SPIE, 3354, 566
Merín, B., et al. 2004, A&A, 419, 301
Monnier, J. D., et al. 2005, ApJ, 624, 832
Muzerolle, J., Calvet, N., Briceño, C., Hartmann, L., & Hillenbrand, L. 2000, ApJ, 535, L47
Muzerolle, J., Calvet, N., Hartmann, L., & D'Alessio, P. 2003, ApJ, 597, L149
Muzerolle, J., Hartmann, L., & Calvet, N. 1998, ApJ, 116, 455
Muzerolle, J., et al. 2006, ApJ, 643, 1003
Najita, J., Carr, J. S., & Mathieu, R. D. 2003, ApJ, 589, 931
Najita, J. R., Strom, S. E., & Muzerolle, J. 2007, MNRAS, 378, 369
Natta, A., Testi, L., Muzerolle, J., Randich, S., Comerón, F., & Persi, P. 2004, A&A, 424, 603
Natta, A., Testi, L., & Randich, S. 2006, A&A, 452, 245
Pontoppidan, K. M., Blake, G. A., van Dishoeck, E. F., Smette, A., Ireland, M. J., & Brown, J. 2008, ApJ, 684, 1323
Prato, L., et al. 2001, ApJ, 549, 590
Pringle, J. E. 1981, ARA&A, 19, 137
Qi, Chunhua, et al. 2004, ApJ, 616, L11
Ratzka, T., Leinert, C., Henning, T., Bouwman, J., Dullemond, C. P., & Jaffe, W. 2007, A&A, 471, 173
Reipurth, B., Pedrosa, A., & Lago, M. T. V. T. 1996, A&AS, 120, 229
Rettig, T.W., Haywood, J., Simon, T., Brittain, S.D., & Gibb, E. 2004, ApJ, 616, L163
Rice, W. K. M., Wood, K., Armitage, P. J., Whitney, B. A., & Bjorkman, J. E. 2003, MNRAS, 342, 79
Rossiter, R. A. 1943, Publications of Michigan Observatory, Vol. 8 (Ann Arbor, MI: University of Michigan Press), 133
Rothman, L. S., et al. 2005, J. Quant. Spectrosc. Radiat. Transfer, 96, 139
Rucinski, S. M., & Krautter, J. 1983, A&A, 121, 217
Ruden, S. P. 1999, in NATO ASIC Proc. 540, The Origin of Stars and Planetary Systems, ed. C. J. Lada & N. D. Kylafis (Dordrecht: Kluwer), 643
Salyk, C., Blake, G. A., Boogert, A. C. A., & Brown, J. M. 2007, ApJ, 655, L105
Sargent, B., et al. 2006, ApJ, 645, 395
Setiawan, J., Henning, T., Launhardt, R., Müller, A., Weise, P., & Kürster, M. 2008, Nature, 451, 38
Shevchenko, V. S., & Herbst, W. 1998, AJ, 116, 1419
Simon, M., Dutrey, A., & Guilloteau, S. 2001, ApJ, 545, 1034
Simon, M., et al. 1995, ApJ, 443, 625
Tanaka, H., Himeno, Y., & Ida, S. 2005, ApJ, 625, 414
Thi, W.-F., van Zadelhoff, G.-J., & van Dishoeck, E. F. 2004, A&A, 425, 955
Tonry, J., & Davis, M. 1979, AJ, 84, 1511
Trilling, D. E., Koerner, D. W., Barnes, J. W., Ftaclas, C., & Brown, R. H. 2001, ApJ, 552, L151
Uchida, K. I., et al. 2004, ApJS, 154, 439
van Boekel, R., Min, M., Waters, L. B. F. M., de Koter, A., Dominik, C., van den Ancker, M. E., & Bouwman, J. 2005, A&A, 437, 189
van Dishoeck, E.F., & Black, J. H. 1988, ApJ, 334, 771
Webb, R. A., Zuckerman, B., Platais, I., Patience, J., White, R. J., Schwartz, M. J., & McCarthy, C. 1999, ApJ, 512, L63
Weinberger, A. J., Becklin, E. E., Schneider, G., Smith, B. A., Lowrance, P. J., Silverstone, M. D., Zuckerman, B., & Terrile, R. J. 1999, ApJ, 525, L53
Weinberger, A. J., Becklin, E. E., Zuckerman, B., Schneider, G., & Silverstone, M. D. 2001, in ASP Conf. Ser. 244,Young Stars Near Earth: Progress and Prospects, ed. R. Jayawardhana & T. Greene (San Francisco, CA: ASP), 75
White, R. J., & Ghez, A. M. 2001, ApJ, 556, 265